Path Integral Monte Carlo Simulations of Semiconductor Quantum Dots and Quantum Wires

by

Lei Zhang

A Dissertation Presented in Partial Fulfillment
of the Requirements for the Degree
Doctor of Philosophy

Approved November 2011 by the
Graduate Supervisory Committee:

John Shumway, Chair
Peter Bennet
Kevin Schmidt
José Menéndez
Jeff Drucker

ARIZONA STATE UNIVERSITY

December 2011

ABSTRACT

The accurate simulation of many-body quantum systems is a challenge for computational physics. Quantum Monte Carlo methods are a class of algorithms that can be used to solve the many-body problem. I study many-body quantum systems with Path Integral Monte Carlo techniques in three related areas of semiconductor physics: (1) the role of correlation in exchange coupling of spins in double quantum dots, (2) the degree of correlation and hyperpolarizability in Stark shifts in InGaAs/GaAs dots, and (3) van der Waals interactions between 1-D metallic quantum wires at finite temperature.

The two-site model is one of the simplest quantum problems, yet the quantitative mapping from a three-dimensional model of a quantum double dot to an effective two-site model has many subtleties requiring careful treatment of exchange and correlation. I calculate exchange coupling of a pair of spins in a double dot from the permutations in a bosonic path integral, using Monte Carlo method. I also map this problem to a Hubbard model and find that exchange and correlation renormalizes the model parameters, dramatically decreasing the effective on-site repulsion at larger separations.

Next, I investigated the energy, dipole moment, polarizability and hyperpolarizability of excitonic system in InGaAs/GaAs quantum dots of different shapes and successfully give the photoluminescence spectra for different dots with electric fields in both the growth and transverse direction. I also showed that my method can deal with the higher-order hyperpolarizability, which is most relevant for fields directed in the lateral direction of large dots.

Finally, I show how van der Waals interactions between two metallic quantum wires change with respect to the distance between them. Comparing the results from quantum Monte Carlo and the random phase approximation, I find similar power law dependance. My results for the calculation in quasi-1D and exact 1D wires include the effect of temperature, which has not previously been studied.

ACKNOWLEDGEMENTS

During my Ph. D. studies at Arizona State University, I have been fortunate to meet a lot of good people whom I list in here. Without their support and help, I could not complete my PhD studies.

First of all, I would like to express my deepest gratitude to my advisor, Prof. John Shumway for his constant support, encouragement, and advice. Professor Shumway always use his support word encouraging me to complete my Ph. D. studies. I am also inspired by his enthusiasm in research work, and feel an honor to work with him.

Secondly, I am very appreciative my committee members, Prof. Kevin Schmidt, Prof. Otto Sankey, Prof. Jeff Drucker, Prof. Peter Bennett, and Prof. José Menéndez, for their assistance and guidance during my research here. I would like to express my gratitude to Prof. John Page who taught me a lot of research knowledge in his graduate classes. Big thanks to the member of my research group and office mate, Jianheng Liu, for his assistance and discussion of my research problem.

Finally, I am grateful to my parents for their love and encouragement. They always believe that I am able to do better in my life.

TABLE OF CONTENTS

LIST OF TABLES

LIST OF FIGURES

Figure Page

Figure Page

Chapter 1

INTRODUCTION

With the continued development of computer processor power and new algorithms, computational physics plays an increasingly important role in physics research. Many kinds of numerical simulation methods have been applied to systems that are too complex for analytic calculation, or where detailed experiments are difficult. Often, results from computer simulations are compared with other analytical results and experimental measurements to serve as a cross-check on the theoretical interpretation. Simulations give researchers new ways to understand physical systems.

1.1 The Quantum Many-Body Problem

A commonly studied quantum many-body system is a collection of interacting electrons and holes in a semiconductor nanostructure. In principle, any non-relativistic many-body systems can be described by a many-body Schrödinger equation. Correlation between interacting particles and Pauli exclusion make the many-body Schrödinger equation too difficult to solve exactly, even using parallel computing technology. Therefore theorists developed high-quality approximation methods to describe many-body systems more accurately. One approach is Quantum Monte Carlo (QMC), a class of computer algorithms that solve the quantum many-body systems using random walks. QMC directly deals with many-body effects, at the cost of statistical uncertainty that can be reduced with more simulation time. For bosons, QMC is a numerically exact

algorithm. For fermions, one must invoke additional approximations.

QMC methods are usually separated into two categories: zero temperature methods and finite temperature methods (Ceperley and Alder, 1986; Foulkes *et al.*, 2001; Hammond *et al.*, 1994). Zero-temperature Monte Carlo techniques—such as variational Monte Carlo and diffusion Monte Carlo—aim to compute properties of the ground state wavefunction of the system. Variational Monte Carlo directly applies the variational principle to approximate the ground state of the system. The accuracy of the calculation depends on the quality of the trial function, and so it is important to optimize the wave-function as near as possible to the ground state. Diffusion Monte Carlo is a high-accuracy method for chemical problems, which captures most correlation energy while scaling more efficiently than common quantum chemistry expansions. The Path Integral Monte Carlo (PIMC) method is a finite temperature technique. It is used to calculate thermodynamic properties such as the internal energy from the thermal density matrix. More discussion about PIMC will be included in Chapter 2.

When I deal with many-body systems in semiconductor nanostructures in this dissertation, I always use the effective mass approximation. Electrons and holes in the semiconductors are quasi-particles with effective mass determined by a quadratic curvature in the small region around the band minimum,

$$m^*_{\mu\nu} = \hbar^2 \cdot \left[\frac{\partial^2 E(k)}{\partial k_\mu \partial k_\nu}\right]^{-1}. \tag{1.1}$$

The notion of an effective mass assumes that the bands are differentiable at the minimum. The electrons and holes interact through Cou-

lomb forces. Within the effective mass approximation, the Hamiltonian for electrons and holes in the semiconductor material is

$$H = \sum_i - \bigtriangledown_\mu \lambda_{i,\mu\nu} \bigtriangledown_\nu + \sum_{i<j} \frac{q_i q_j}{\epsilon |r_i - r_j|}, \tag{1.2}$$

where $\lambda_{i,\mu\nu} = \hbar^2/2m^*_{\mu\nu}$is the inverse effective mass tensor of the ith particle, q_i is the charge of the particle i, and ϵ is the dielectric constant of the semiconductor.

1.2 Nanostructures

Most of the interest in semiconductors is not in their bulk properties, but rather in heterogeneous structures. Semiconductor quantum dot systems have generated great interest because they can be regarded as ideal quasi-zero-dimensional systems with fully quantized, discrete energy spectra of electrons and holes, which can be used to study excitons as well as many well known effects from atomic physics. I study two types of dots: electrostatically gated dots and self-assembled InGaAs/GaAs dots. Quantum wires, which confine electrons in a one-dimensional structures, are also of interest, and I consider a generic model applicable to GaAs wires and carbon nanotubes.

GaAs is a III/V semiconductor used in the manufacture of devices such as infrared light-emitting diodes, laser diodes, and solar cells. The crystal structure of GaAs is zinc blende with a lattice constant 0.565 nm. At room temperature, GaAs has a direct 1.4 eV band-gap, which can be used to emit light efficiently. GaAs is often used for experiments and devices because of its good optical properties and the ability to make high-quality, defect-free materials.

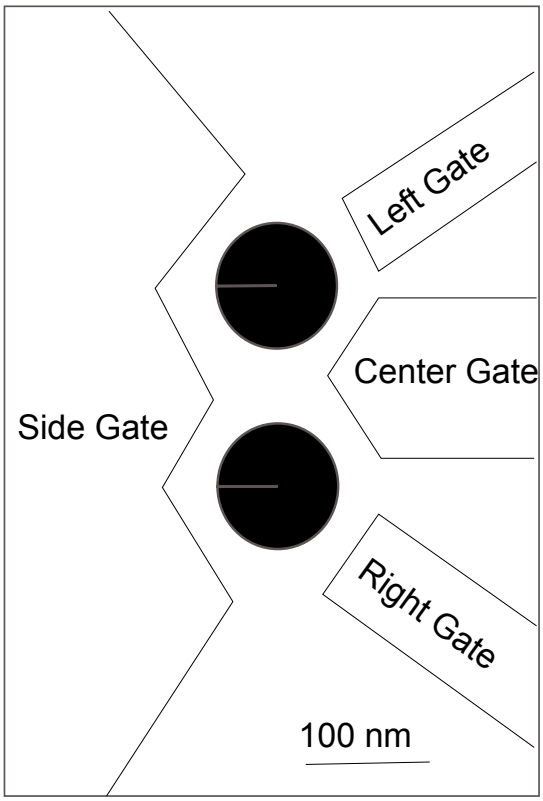

Figure 1.1: Simple sketch for double quantum dots in experiments related to our calculations. This is a top view: the negatively charged gates deplete a 2DEG, leaving quantum dots and connecting channels. The black circles mark the region of the quantum dots, which can trap single electrons.

Gated GaAs Quantum Dots

First I briefly discuss the AlGaAs/GaAs two dimension electron gas (2DEG). A 2DEG is a gas of electrons free to move in two dimensions, but tightly confined in the third, growth direction. This tight confinement leads to quantized energy levels for motion in the growth direction, which can then be ignored for most problems. A 2DEG can be used in high-

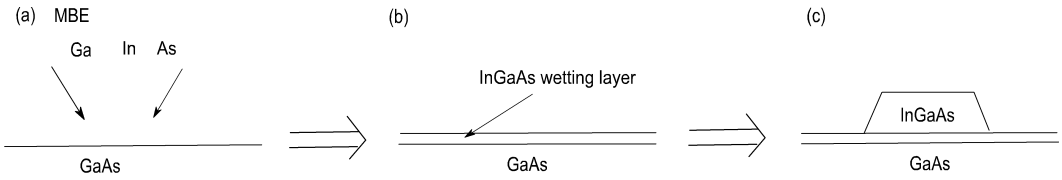

Figure 1.2: This sketch illustrates how the self-assembled quantum dots are grown in experiments. (a) In, Ga, and As atoms are deposited on a clean GaAs substrate using molecular beam epitaxy, (b) the InGaAs material wets the suface, as a strained wetting layer, (c) after a critical thickness is reached, strain causes new material to grow as islands, in the Stransti-Krastanov growth mode. Typical coherent self-assembled dots vary from 15 nm to 40 nm, depending on growth conditions.

electron-mobility-transistors, (HEMTs), which are field-effect transistors that utilize the heterojunction between AlGaAs and GaAs materials to confine electrons to a triangular quantum well. Electrons confined to the heterojunction of HEMTs exhibit higher mobilities than those in metal-oxide-semiconductor field-effect transistor. Thin electrodes placed above the AlGaAs/GaAs quantum well (illustrated in Fig. 1.1) can produce both single quantum dots (Ashoori *et al.*, 1992, 1993) and arrays of dots (Hansen *et al.*, 1989; Lorke and Kotthaus, 1990). Fig. 1.1 illustrates how double quantum dots system looks like in double-dot experiments that we simulate in Chapter 3.

InGaAs / GaAs self-assembled Quantum Dots

In experiments, InGaAs alloy material grown on a GaAs substrate can form self-assembled quantum dots spontaneously under certain conditions during molecular beam epitaxy. This is because InGaAs is not lattice matched to the GaAs substrate, having a lattice content up to 7% larger than GaAs in the case of pure InAs. The resulting strain produces islands on top of a two-dimensional wetting layer, as illustrated

in Fig. 1.2. This growth mode is called Stranski-Krastanov growth. The InGaAs islands can be buried with more GaAs to form self-assembled quantum dots. There are several direct experimental methods—such as Scanning Tunneling Microscopy (STM), Transmission Electron Microscopy (TEM), and X-ray diffraction—that provide some information about the composition of the quantum dots, but all these methods have the disadvantage of either being destructive or being limited to dots on the surface. The development of single-dot spectroscopy exposes the optical properties of individual quantum dots under the influence of external electric field. Charged and neutral exciton recombination has been observed in the photoluminescence (PL) spectra of single InGaAs quantum dots (Finley *et al.*, 2001; Reimer *et al.*, 2008; Finley *et al.*, 2004; Fry *et al.*, 1999a,b; Barker and O'Reilly, 2000). Photoluminescence excitation (PLE) spectra show that the charged excitons are created only for excitation in the barrier or cladding layers of the structure. whereas the neutral excitons shows well-defined excitation features for resonant excitation of the dot. Fig. 1.2 illustrates how self-assembled quantum dots are grown in experiments.

Quantum wires and Carbon Nanotubes

Much like gated quantum dots, electrostatic confinement on the 2DEG in one lateral direction of an AlGaAs/GaAs quantum well can produce a 1D quantum wire. If the density of electrons is sufficiently high to occupy several lateral excitation states, it generates a quasi-1D wire. When the width of wire is changed to confine the electron in a single subband, it generates a true 1D wire (Meirav and Kastner, 1989). I

have simulated both of these two kinds of wires have been simulated in my research work.

It is also possible to make quantum wires using metallic carbon nanotubes. Carbon nanotubes (CNTs) are carbon materials with a cylindrical nano-structure. Due to their extraordinary electrical properties, carbon nanotubes may have many applications in nano-structure devices (Baughman *et al.*, 2002; Tans *et al.*, 1998). Single-walled nanotubes (SWNTs) are an important kind of carbon nanotube with diameter of about 1 nm and a tube length that can be many millions of times longer. The structure of a SWNT can be considered as wrapping a graphene layer into a cylinder represented by a pair of indices (n,m). The properties of SWNTs change significantly with the (n,m) values (Martel *et al.*, 2001). For example, their band gap can vary from zero to about 2 eV, and their electrical conductivity can behave in a metallic or semiconducting behavior.

1.3 Path Integral Monte Carlo Simulations

For my Ph. D. research work, I have applied the PIMC method to different quantum systems. The detailed formation of PIMC technique will be discussed in Chapter 2; in this section I briefly talk about some advantages and challenges for this technique.

Using path integral Monte Carlo methods to simulate bosons system has been very successful, with many applications to He^4 (Ceperley, 1995). When applied to fermions, the PIMC method introduce minus signs into some terms of the partition function, which exponentially decrease the efficiency of simulations, especially for systems with large

number of fermions at low temperatures. This is called the "fermion sign problem," and is one of the biggest challenges for the PIMC technique and other many body methods. For ground state QMC, the fixed-node approximation was invented to overcome the fermion sign problem (Anderson, 1975, 1995). This method has been successfully applied to ground state simulations of molecules and solids (Foulkes *et al.*, 2001; Grossman, 2002; Williamson *et al.*, 2001; Ortiz *et al.*, 1993). The restricted path approximation (Ceperley, 1992; Magro *et al.*, 1995; Militzer and Pollock, 2000; Pierleoni *et al.*, 1994) has been applied to finite temperature PIMC calculations to manage the fermion sign problem. In the fixed-node approximation, one "reference slice" in imaginary time is selected, and the fixed-node constraint is evaluated from that slice. In Chapter 5, I use the fixed node approximation to simulate fermions in quantum wires.

In the theory of many-body systems, time correlation functions play an important role in the calculation of dynamic processes, such as transport properties, spectroscopic line shapes, and neutron and light scattering spectra (Thirumalai and Berne, 1983). PIMC is one of the methods that can be used to obtain time correlation functions. With PIMC, I can directly collect imaginary-time correlation functions of the many-body systems. Real-time correlation functions require analytic continuation from imaginary time (Baym and Mermin, 1961; Jarrell and Biham, 1989; Thirumalai and Berne, 1991). Often, it is very difficult to numerically perform the analytic continuation, so it is useful to calculate physical properties directly from the imaginary time correlation functions, without making analytic continuation to real time. In Chapter 4,

I use the imaginary time correlation functions to get the polarizability and hyperpolarizability of the systems.

1.4 Overview of Dissertation

This dissertation focus on the theoretical study of three quantum systems: (1) the effect of correlation in exchange coupling of spins in double quantum dots, (2) the role of correlation and hyperpolarizability on Stark shifts in InGaAs / GaAs dots, and (3) van der Waals interaction between quantum wires.

Correlation in exchange coupling of spins in double quantum dots

In the past twenty years, many papers (Divincenzo, 1995; Bennett, 1995; Barenco *et al.*, 1995; Turchette *et al.*, 1995) have clarified both the theoretical potential and the experimental challenges of quantum computation. In quantum computation, the state of each bit is allowed to be any quantum mechanical state of a two-level quantum system (qubit). However, it is extremely difficult to achieve the conditions for quantum computation, which require precise control of Hamiltonian operations on well-defined two-level quantum systems and a very high degree of quantum coherence. The possibility of coherent manipulation of electron spins in low-dimensional nanostructures presents a need for deep understanding of spin interaction. The exchange coupling between the spins of electrons in tunnel-coupled quantum dots has been envisioned as one of the controllable mechanisms for coherent manipulation of spin qubits (Loss and DiVincenzo, 1998). Recently, many numerically exact calculations have been provided to study the exchange coupling between electron spins confined by double quantum dots.

With collaborators, I have developed a simple and elegant PIMC algorithm to calculate the exchange energy J in a double parabolic potential quantum dots. My J values are in a good agreement with the numerically exact technique given by Pedersen *et al.* (2007). The hopping constant t and renormalized on-site energy $U_r - V_r$ are also calculated, these differ significantly with traditional Hubbard model results. I have the double occupation density in quantum dots and clearly see the effect of an instanton, when electrons hop between dots. I also plot the correlation holes from the PIMC simulation, and compared with my collaborator Jesper Pedersen's direct diagonalization calculations, in order to deeply understand the presence of electron correlation during tunneling. Finally, I apply magnetic fields to the systems, and calculate the exchange energy J with different magnetic field. I show that J becomes negative when the system is in a higher magnetic field, which confirms the validity of this PIMC method.

Correlation and hyperpolarizability on

Stark shifts in InGaAs/GaAs dots

The quantum confined Stark effect (Bennett and Patel, 2010; Leitsmann and Bechstedt, 2009) is the electric-field dependent shift of the photoluminescence energies in single quantum dots. It has been exploited to produce electro-optical devices, since the photon absorption based on the quantum confined Stark effect in quantum wells is one of the most efficient processes for making optical modulators and self-electro optic effect devices (Sanguinetti *et al.*, 2000). Theoretical predictions show that the light-emitting diodes (LEDs) or laser diodes (LDs) with quantum dots in the active layer will lead to improved optical characteristic such as low threshold current and weak temperature dependence of the threshold current (Widmann *et al.*, 1998). The analysis of the Stark shift of excitons in quantum dots (Raymond *et al.*, 1998) helps reveal the electron and hole charge distribution in the dot. For example, the permanent dipole moment caused by electron and hole wavefunction separation has been measured in experiments (Fry *et al.*, 1999a; Barker and O'Reilly, 2000). Many calculations about the exciton structure in quantum dots have been performed (Gerardot *et al.*, 2007; Kadantsev and Hawrylak, 2010). In the absence of structural information of quantum dot shape (Tablero, 2009), dots are often modeled with pyramidal shapes, but in many cases the dots are closer to lens and truncated-cone shapes (Fry *et al.*, 1999a). There are theoretical calculations that indicate that the electron ground state energy level is weakly affected by vertical fields but is strongly affected by the lateral electric fields (Li

and Xia, 2000; Kadantsev and Hawrylak, 2010). One-band electron and hole Hamiltonian calculations show that the hole center of mass is below the electron center of mass in a constant composition dot. For a graded composition with the In composition increasing from the bottom to the top of the dot, the sign of the electron-hole dipole will be opposite (Barker and O'Reilly, 2000).

I simulated exciton and biexciton binding in different electric field strengths in a 2-D parabolic confinement, which is a good approximation for a real dot. I compared my results with Korkusinski and Reimer (2009), which used configuration interaction method with six basis states of harmonic oscillator. Then, I generated four InGaAs/GaAs quantum dots with different shape and In composition, and simulate the exciton (1e1h), trion (1e2h,or 2e1h), and biexciton (2e2h) states in these quantum dots. In order to get the recombination energy spectrum as a function of applied electric field, I directly calcuated the energy, dipole moment, polarizability, and hyperpolarizability of the systems with zero electric field before and after recombination, and expressed the photoluminescence energy in terms of these quantities. I also directly simulated exciton and biexciton energies with an applied electric field to check my calculations. Finally I considered the piezoelectric potential in these dots, and showed that there exist asymmetry of polarizability in the x-y plane.

Van der Waals interactions in quantum wires

Dispersion interactions are significant in soft matter (Rydberg *et al.*, 2003b) and many nanostructures. One-dimension conductors such as

carbon nanotubes are essential components of many proposed nanotechnological devices, and they are currently the subject of numerous experimental and theoretical studies (Girifalco *et al.*, 2000). In recent theoretical studies, it was shown that the form of the van der Waals interaction between pairs of distant parallel thin conducting wires assumed in many models of metallic carbon nanotubes is qualitatively wrong. A common approach used to calculate the van der Waals interaction between two objects is to consider the pairwise interactions between volume elements with an attractive form of $U_{dd}(r) \propto r^{-6}$, which is the van der Waals interaction between two dipoles. Summing the interaction over a pair of 1D parallel wires separated by a distance r leads to a binding energy of $U(r) \propto r^{-5}$. This pairwise van der Waals model is appropriate for insulators or for metallic wires whose radius is greater than the screening length. However, for a thin metallic conductor such as a single-walled carbon nanotube the method is not appropriate. In the last several years, other researchers used the random phase approximation (RPA) (Dobson *et al.*, 2006) to consider the zero-point energy of the delocalized, coupled, one-dimensional plasmon modes with wave number parallel to the long axis. They found that the van der Waals binding energy, calculated by summing of zero-point plasmon energies, falls approximately as (Dobson *et al.*, 2006),

$$U(r) \approx -\frac{\sqrt{r_s}}{16\pi r^2[\log(2.39r/b)]^{3/2}}. \tag{1.3}$$

In the above equation, b is the radius of the wire, r is the distance between two wires and $2r_s$ is the average length which contain one electron. The ground state QMC method has used to simulate the same

system (Drummond and Needs, 2007) and verify the RPA result in zero temperature.

I have the density-density correlation function from PIMC simulations to directly calculate the Coulomb interaction between two 1-D wires in different separation and temperature. By comparing my result with the RPA (Dobson and Wang, 1999) and QMC (Drummond and Needs, 2007) results, I have investigated the temperature effect on van der Waals interaction.

Chapter 2

PATH INTEGRAL MONTE CARLO TECHNIQUE

In this chapter, I briefly review the path integral Monte Carlo (PIMC) simulation method, which include Feynman's path integral theory, quantum statistical mechanics, and the Metropolis algorithm for high-dimensional integration.

Feynman's paths integral formulation of quantum statistical mechanics is a very useful method to describe the quantum many-body systems (Feynman, 1972). Mapping a quantum mechanical system onto a classical model of interacting "polymers" gives us a different view of many-body phenomena, such as Bose condensation (Feynman, 1953) and superfluidity (Ceperley, 1995).

There are several advantages for calculating physical properties of many-body systems with PIMC simulations. First of all, unlike variational Monte Carlo and diffusion Monte Carlo, which usually sample particles at zero temperature, the PIMC method uses the canonical ensemble thermal density matrix to evaluate the thermal properties of the quantum mechanical systems. Second, since this method is a many-body formalism, no single particle approximations are made, thus correlation effects are included automatically. Finally since the path integral method naturally averages over all quantum and thermal fluctuations, I can directly calculate the observables in canonical ensemble rather than finding the many-body wavefunctions for each eigenstate.

2.1 Thermal Density Matrix

All static properties of a quantum mechanical system in thermal equilibrium state can be obtained from the thermal density matrix (Feynman, 1972). In this section, I discuss the mathematical properties of the density matrix and the relationship between the thermal density matrix, path integrals, and quantum mechanical observables.

Suppose that we have a quantum many-body system with Hamiltonian $\hat{H}$, and that we also know that that the eigenstates and eigenvalues of the system are ϕ_i and E_i, respectively. When the system is in thermal equilibrium at temperature T, in the canonical ensemble, the probability that the system occupies state i is $\frac{1}{Z}e^{-\beta E_i}$, where the partition function is

$$Z = \sum_i e^{-\beta E_i}, \tag{2.1}$$

and $\beta = 1/k_B T$. In basis-independent notation, the thermal density matrix can be written as,

$$\hat{\rho} = \frac{1}{Z} e^{-\beta H}, \tag{2.2}$$

where the partition function $\boldsymbol{Z}$ is needed for normalization. Hence the thermal expectation value of an operator $\hat{\mathcal{O}}$ at temperature T is

$$\langle \hat{\mathcal{O}} \rangle = tr(\rho \mathcal{O}) = \frac{1}{Z} \sum_i \langle \phi_i | \mathcal{O} | \phi_i \rangle e^{-\beta E_i}. \tag{2.3}$$

From the equation above, the matrix elements of the density matrix in the position representation are,

$$\rho(R, R'; \beta) = \frac{1}{Z} \langle R | e^{-\beta H} | R' \rangle = \frac{1}{Z} \sum_i \phi_i(R) \phi_i(R') e^{-\beta E_i}, \tag{2.4}$$

where $R = (\boldsymbol{r}_1, \boldsymbol{r}_2, \ldots, \boldsymbol{r}_N)$ represents the position coordinates of all the particles. Thus, when expressed in position representation, the expectation value of $\mathcal{O}$ becomes

$$\langle \mathcal{O} \rangle = \int dR dR' \rho(R, R'; \beta) \langle R|\mathcal{O}|R' \rangle. \tag{2.5}$$

2.2 Path Integrals and Quantum Mechanics

Using properties of the exponential function, the thermal density matrices at a lower temperature can be expressed as a product of two density matrices at higher temperature,

$$e^{-(\beta_1+\beta_2)H} = e^{-\beta_1 H} e^{-\beta_2 H}, \tag{2.6}$$

In the position representation, this becomes,

$$\langle R_1|e^{-(\beta_1+\beta_2)H}|R_3\rangle = \int dR_2 \langle R_1|e^{-\beta_1 H}|R_2\rangle \langle R_2|e^{-\beta_2 H}|R_3\rangle. \tag{2.7}$$

Using this property M times, the density matrix at temperature T in terms of the product of M short time propagators,

$$\begin{aligned} \rho(R, R'; \beta) = \frac{1}{Z} \int dR_1 dR_2 \ldots dR_{M-1} \, \langle R|e^{-\frac{\tau H}{\hbar}}|R_1\rangle \langle R_1|e^{-\frac{\tau H}{\hbar}}|R_2\rangle \\ \cdots \langle R_{M-1}|e^{-\frac{\tau H}{\hbar}}|R'\rangle, \end{aligned} \tag{2.8}$$

where the time step is $\tau = \beta\hbar/M$. When M goes to infinity, this becomes a continuous path connecting position R and R' between imaginary time 0 to $\beta\hbar$.

Usually the Hamiltonian consists of two parts, $H = T + V$, where T and V are the kinetic and potential parts of the Hamiltonian. For small τ, we can approximate,

$$e^{-\frac{\tau}{\hbar}(T+V)+\frac{\tau^2}{2\hbar}[T,V]} \approx e^{-\frac{\tau}{\hbar}T} e^{-\frac{\tau}{\hbar}V}. \tag{2.9}$$

When $\tau \to 0$, the τ^2 term on the left side is much smaller than the other terms, so it can be neglected and gives us the primitive approximation,

$$e^{-\frac{\tau}{\hbar}(T+V)} \approx e^{-\frac{\tau}{2\hbar}V} e^{-\frac{\tau}{\hbar}T} e^{-\frac{\tau}{2\hbar}V}. \tag{2.10}$$

According the Trotter expansion,

$$e^{-\beta(T+V)} = \lim_{M\to\infty} [e^{-\frac{\tau}{\hbar}T} e^{-\frac{\tau}{\hbar}V}]^M. \tag{2.11}$$

In position space, the primitive approximation becomes,

$$\langle R_1|e^{-\frac{\tau}{\hbar}H}|R_3\rangle = \int dR_2 \langle R_1|e^{-\frac{\tau}{\hbar}T}|R_2\rangle \langle R_2|e^{-\frac{\tau}{\hbar}V}|R_3\rangle \tag{2.12}$$

Since the potential operator is always diagonal in position representation,

$$\langle R_2|e^{-\frac{\tau}{\hbar}V}|R_3\rangle = e^{-\frac{\tau}{\hbar}V(R_2)}\delta(R_2 - R_3) \tag{2.13}$$

The kinetic part can be evaluated using the eigenfunction expansion of T. Thus,

$$\langle R_1|e^{-\frac{\tau}{\hbar}T}|R_2\rangle = (4\pi\lambda\tau/\hbar)^{-3N/2} \exp\left[-\frac{(R_1 - R_2)^2}{4\lambda\tau/\hbar}\right], \tag{2.14}$$

where $\lambda = \frac{\hbar^2}{2m}$. Using the expression above, the discrete path-integral expression for thermal density matrix in the primitive approximation is,

$$\begin{aligned}\rho(R_0, R_M; \beta) =& \frac{1}{Z(4\pi\lambda\tau/\hbar)^{3NM/2}} \int dR_1 dR_2 \ldots dR_{M-1} \\ & \times \exp\left[-\sum_{m=1}^{M}\left(\frac{(R_{m-1} - R_m)^2}{4\lambda\tau/\hbar} + \frac{\tau}{\hbar}V(R_m)\right)\right]\end{aligned} \tag{2.15}$$

Taking the limit $M \to \infty$, this equation becomes the path integral equation.

$$\rho(R, R'; \beta) = \frac{1}{Z}\int \mathcal{D}R(\tau) e^{-S_E[R(\tau)]/\hbar}. \tag{2.16}$$

The symbol $\mathcal{D}R(\tau)$ in the integral means the sum over all random walks $R(\tau)$ taking place in imaginary time τ, starting at R' at imaginary time $\tau = 0$ and ending at R at imaginary time $\tau = \beta\hbar$. The paths are weighted by the Euclidean action $S_E[R(\tau)]$, which is the functional of the path $R(\tau)$,

$$S_E = \int_0^{\beta\hbar} d\tau \left[\sum_{i=1}^{N} \frac{1}{2} m_i \left(\frac{dR_i(\tau)}{d\tau} \right)^2 + V\big(R(\tau)\big) \right]. \tag{2.17}$$

In this thesis I only calculate the expectation value of physical properties, $\mathrm{tr}(\rho\mathcal{O})$ that are diagonal in the position representation, so the path integral expression will start and end at the same coordinate R and form a closed loop.

2.3 Bosonic Simulations And Fermion Sign Problem

Eq. (2.15) can be applied to many-body systems in which all particles are distinguishable. However in many quantum mechanical systems with identical bosons and fermions, I need to consider the symmetry under exchange of identical particles. For particles of Bose and Fermi statistics, if I label the particles with $1, 2, \cdots N$, I must use symmetric or anti-symmetric states in the PIMC formation. Paths of identical particles are allowed to close on each other, which generates the path permutation terms in the path integral,

$$\rho(R, R'; \beta) = \frac{1}{Z} \frac{1}{N!} \sum_{P} (\pm 1)^P \int_{\substack{R(0) = R' \\ R(\beta\hbar) = PR}} \mathcal{D}R(\tau) e^{-\frac{1}{\hbar} S_E[R(\tau)]}. \tag{2.18}$$

In Eq. (2.18), the sign is " $+1$" for bosons, and " -1" for fermions. The physical properties of bosonic systems, such as liquid helium-4, can be evaluated by directly Monte Carlo sampling to add the contributions

from all permuting paths (Ceperley, 1995), since the permutation terms in Eq. (2.18) are positive for all path configurations. If the path can be sampled efficiently, including all permutations, PIMC can be a numerically exact method for bosonic systems.

For the case of fermions, odd permutations in paths will give a negative sign in path integral. This causes a big problem in calculating the path integral for fermions. If I directly sum over all permutation terms, because of the cancelation of positive and negative permutations, there is a tremendous loss of efficiency. Especially for systems at low temperature with large numbers of particles, the computational efficiency goes to zero rapidly. The majority of the signal cancels but the noise is still large. This difficulty is known as the fermion sign problem, and it also exists in other formulation of quantum mechanics, not just path integrals. An approximation called restricted path integral method (Ceperley, 1991, 1992) can be used to manage this problem. This approximation maps the fermions back to the solvable boson problem, and has been successfully applied to hydrogen plasmas and electron-hole systems. In this method, I use a trial density matrix density matrix taken from the single-particle density matrix of non-interacting particles. If $\rho_T(R(\tau), R(\tau + \beta\hbar/2); \beta\hbar/2) = 0$ for any time τ, then the path crossed a nodal surface, and the configuration is rejected. In Chapter 5, I use this approximation to simulation electrons in nanowires.

2.4 Path Integral Monte Carlo Method

Now I have shown how to map a quantum system onto a classical ensemble of paths. Next I show how to use Metropolis sampling method

(Metropolis *et al.*, 1953) to sample the properties of the paths, to get the thermal physical properties of a quantum system. Monte Carlo methods use random numbers to deal with a stochastic process, which is a sequence of states determined by random events (Kalos and Whitlock, 1986). Before talking about the sampling method, for convenience, I introduce some new notation for describing the density matrix. For discrete path integral, the time step is defined as $\tau \equiv \beta/\hbar M$ and $R_k = \{r_{1,k}, \ldots r_{N,k}\}$ is the kth time slice. A link is a pair of time slice(R_{i-1}, R_i), thus the link action is defined as minus the logarithm of the density matrix

$$S^i \equiv -\ln[\rho(R_{i-1}, R_i; \tau)]. \tag{2.19}$$

Then the path integral expression becomes

$$\rho(R_0, R_M; \beta) = \int dR_1 dR_2 \ldots dR_{M-1} \exp\left[-\sum_{i=1}^{M} S^i\right]. \tag{2.20}$$

I can separate kinetic action from the other action, and the kinetic action of link i is

$$K^i = \frac{Nd}{2}\ln(4\pi\lambda\tau) + \frac{(R_i - R_{i-1})^2}{4\lambda\tau}. \tag{2.21}$$

The remain part of the action is called inter-action, $U^i = S^i - K^i$, which contain all interesting interaction.

$$U^i = \frac{\tau}{2}[V(R_{i-1}) + V(R_i)]. \tag{2.22}$$

The path integral samplings are done with a generalization of the Metropolis *et al.* rejection algorithm, which is a particular type of Markov chain. It generates a random walk through path configuration space $\{x_0, x_1, x_2, \ldots\}$, according to a fixed transition rule, $P(x \to x')$. If the

transition is ergodic, which means one can move from any configuration to any other configuration in a finite number of steps with nonzero probability. I define that $\pi(x)$ is the probability distribution function of all path configurations in equilibrium state, and $P(x \to x')$ is the probability of transition from state x to state x'. The transition probabilities can be set up so that they satisfy the detailed balance: the number of moves from configuration x to another configuration x' is exactly equal to the number of reverse move

$$\pi(x)P(x \to x') = \pi(x')P(x' \to x) \tag{2.23}$$

The Metropolis method is used to ensure that the transition rules satisfy detailed balance. I can split the transition probability $P(x \to x')$ into two parts;

$$P(x \to x') = T(x \to x')A(x \to x') \tag{2.24}$$

Where $T(x \to x')$ is the probability of a trial move and $A(x \to x')$ is an acceptance probability. Then the acceptance probability is

$$A(x \to x') = \min\left[1,\ \frac{\pi(x')T(x' \to x)}{\pi(x)T(x \to x')}\right] \tag{2.25}$$

It is easy to verify detailed balance with this definition.

2.5 Single Slice Sampling and Multi-Slice Sampling

Now that I have shown the principles of the Metropolis sampling method, I apply these principles to my PIMC simulation. First I consider how to deal with the simplest move: move a single slice on the path. This is the elementary operation of the path integral algorithm. The problem is that I need to move a slice $\boldsymbol{R}_k$ at time τ with fixed neighbor slice $\boldsymbol{R}_{k-1}$

and $\boldsymbol{R}_{k+1}$ with imaginary time 0 and 2τ respectively. In this move, what I choose the probability of a trial move is

$$T(\boldsymbol{R} \to \boldsymbol{R}') \propto \exp\left[-\frac{(\boldsymbol{R}' - (\frac{\boldsymbol{R}_{k-1}+\boldsymbol{R}_{k+1}}{2}))^2}{2\lambda\tau} \right] \tag{2.26}$$

This distribution is a Gaussian function with center $\frac{\boldsymbol{R}_{k-1}+\boldsymbol{R}_{k+1}}{2}$ and standard deviation $\sqrt{\lambda\tau}$, which is the free particle density matrix component. Then I choose the probability distribution function $\pi(\boldsymbol{R})$ be:

$$\pi(\boldsymbol{R}) \propto \rho(\boldsymbol{R}_{k-1}, \boldsymbol{R}; \tau)\rho(\boldsymbol{R}, \boldsymbol{R}_{k+1}; \tau) \tag{2.27}$$

where $\rho(\boldsymbol{R}_{k-1}, \boldsymbol{R}; \tau)$ is the real system propagator with all interaction terms. If I have free particle system, then I will always have an acceptance probability $A(R \to R') = 1$, which means all the moves are accepted. From the trail move function, I can see that the average displacement of this move is $\sqrt{\lambda\tau}$. When the value of τ decreases (since I need the primitive approximation to be accurate), the diffusion of the move in configuration space becomes much slower. If I have M slices in a path integral simulation, I find that the computer time needed to change the overall shape of a path using single slice move is proportional to M^3. This is a very inefficient way to do the simulation. This is the reason why I need other kinds of move to achieve faster convergence in the PIMC simulation.

Multilevel Monte Carlo sampling method is an efficient method which can efficiently move multi-slices and many particles. Here I use the multilevel bisection algorithm to accomplish the multi-slices move. First I select $m - 1 = 2^k - 1$ slices ($R_{i+1}, R_{i+2}, \ldots, R_{i+m-1}$), which have fixed ending points R_i and R_{i+m}. The integer number k is called the level of the

move in my simulation. Then I first move the middle slice $R_{i+m/2}$ of the paths I selected, using the same method as single particle move. The only difference is that now I have large move step equals to $\sqrt{2^{k-1}\lambda\tau}$. If this move is accepted, I just fix the middle slice $R_i + m/2$ and move the middle slices ($R_{i+m/4}$ and $R_{i+3m/4}$) of two small interval(from R_i to $R_{i+m/2}$, and from $R_{i+m/2}$ to R_{i+m}). I repeat the procedure above until the final move of slices $(R_{i+1}, R_{i+3}, \ldots, R_{i+m-1})$. I can only generate a new path when all the moves of all level are accepted, otherwise I should start from the initial path and move the middle slices of the total slices I selected. The efficiency of this method comes from the fact that coarse movements (move slice $R_{i+m/2}$) are accepted or rejected before the fine movements (move slice $(R_{i+1}, R_{i+3}, \ldots, R_{i+m-1})$) are operated, so time is not spent on the moves that will finally be rejected.

2.6 Permutation Sampling and Heat-Bath Transition

As mentioned above, when I simulate boson or fermion systems, identical bosons and fermions can be exchanged which leads to the permutation of the paths. In order to make the sampling ergodic, I must introduce permutation sampling. When I use the multilevel sampling method to generate a new path, I add a step to sample the permutation. I can think the permutation sampling is the first level of multilevel sampling.

Since permutation space is discrete space, I can use an algorithm, heat-bath transition probability. First I define the neighborhood, $N(x)$, of a state x as all the other states x' which can move to state x in only one step. From the definition, I conclude that if x is the neighbor of x', then x' is also the neighbor of x. In the heat-bath rule, the transition probability

from the neighbor of one state to the state itself is proportional to the equilibrium probability distribution

$$T(x \to x') = \frac{\pi(x')}{C(x)} \tag{2.28}$$

where $C(x)$ normalized the probability,

$$C(x) = \sum_{x'' \in N(x)} \pi(x''). \tag{2.29}$$

If I put Eq. (2.28) to Eq. (2.25) I will get the acceptance probability be

$$A(x \to x') = \min\left[1, \frac{C(x)}{C(x')}\right] \tag{2.30}$$

If state x and x' have the same neighbor then the acceptance probability will be one, all moves are accepted. Using the heat-bath transition rules I can get the transition probability for a permutation state is

$$T(P) \propto \rho(R_i, PR_{i+m}), \tag{2.31}$$

where P include all permutation of n particles. Since potential terms are symmetric under particle permutation, the transition probability $T(P)$ is only dependent on kinetic terms. So I can generate a matrix which include all transition probability within the neighborhood,

$$t_{k,j} = \exp[-(R_{k,i} - R_{j,i+m})^2/(4m\lambda\tau)]. \tag{2.32}$$

The probability of a permutation of l particles with labels $\{k_1, k_2, \ldots, k_l\}$ is

$$T(P) \propto t_{k_1,k_2} t_{k_2,k_3} \ldots t_{k_l,k_1}. \tag{2.33}$$

Besides multilevel sampling, permutation sampling, I also use some other sampling methods depending on the system I simulate. All these sampling methods are used to make the simulation converge faster as well as the state be ergodic.

2.7 Physical Properties Calculation

When finishing the sampling parts, I are ready to calculate the thermal expectation values. In this section, I discuss some estimators for various physical quantities. I need to express the quantum expectation value of the density matrix as an average over a path.

Physical properties can be calculated in many different ways. A specific formula used to calculate these properties is called an estimator. It is straightforward to calculate estimators of scalar operators, such as the potential energy, the density, and pair correlation function which I will use in the following chapter. They are simply averages over the paths. Since all the time slices are equivalent, the average density is:

$$\rho(r) = \frac{1}{M}\sum_{i,t}\langle\delta(r - r_{i,t})\rangle, \tag{2.34}$$

where $r_{i,t}$ is the coordinate of particle i at imaginary time t and M is the total number of slices.

Other interesting physical properties, such as the energy, are not as straightforward to calculate. As I all know, energy is one of the main properties that I want to get from a simulation. There are a variety of ways of estimating the energy. What I used in the following chapter is the one called thermodynamic estimator. The energy of this estimator is obtained by differentiating the partition function with respect to β,

$$E_T = -\frac{1}{Z}\frac{dZ}{d\beta}. \tag{2.35}$$

Apply the derivative to link i, and interpret the ration as an average over imaginary time path, I can get

$$E_T = \left\langle \frac{3N}{2\tau} - \frac{(R_i - R_{i-1})^2}{4\lambda\tau^2} + \frac{dU^i}{d\tau} \right\rangle. \tag{2.36}$$

2.8 Summary

In this chapter, I have explained details of the path integral Monte Carlo method, and how I used it to calculate physical properties. In chapter 3–5 I use PIMC method as a "black box", specifying the temperature, particle masses, interaction, spins and boundary condition of the quantum many body systems, and calculate estimators of various observables with error bars.

Chapter 3

DOUBLE QUANTUM DOTS

In this chapter, I explore exchange coupling of a pair of spins in a double dot using the frequency of exchanges in a bosonic path integral, evaluated with Monte Carlo. The algorithm gives insights into the role of correlation through visualization of two-particle probability densities, instantons, and the correlation hole. I map the problem to a Hubbard model and see that exchange and correlation renormalize the model parameters, dramatically reducing the effective on-site repulsion at larger separations. This work is based on the paper "A Path integral study of the role of correlation in exchange coupling of spins in double quantum dots and optical lattices." My role in this paper was performing all the path integral simulation for the double dot systems. My co-author Jesper Goor Pedersen, a Ph. D. student at the Technical University of Denmark, performed the direct diagonalization calculations and helped write the paper.

3.1 Introduction

I use path integral Monte Carlo (PIMC) to extract accurate singlet-triplet splitting from a spatial model. Similar PIMC algorithms have been used to study spin dynamics in ^{3}He (Thouless, 1965; Roger, 1984; Ceperley and Jacucci, 1987) and Wigner crystals (Roger, 1984; Bernu *et al.*, 2001), and the approach is particularly simple for two-site models. This two-particle problem has been previously solved with direct diagonalization (DD) methods with a careful choice of basis functions (Helle

et al., 2005; Pedersen *et al.*, 2007) and is amenable to variational or diffusion quantum Monte Carlo (QMC) (Ghosal *et al.*, 2006). However, the simple and elegant PIMC approach is a more direct solution without variational bias or basis-set issues and offers theoretical insights into this important problem. I first show that the splitting energy, J, is easily extracted from the average permutation of the two-particle path integral, even when $J \ll k_B T$. This PIMC algorithm is a good method, which provide accurate numerical results of J for models of dots. More importantly, PIMC allows us to see the phenomenon of quantum correlation. A possible question is: do the particles exchange across the barrier simultaneously, or do they briefly double occupy the dot? Or, does the motion of one particle over the barrier correlate with the location of the other particle? I answer these questions by viewing representative trajectories (instantons) for a double dot and calculating pair correlation functions. Magnetic fields are known to modulate J (Burkard *et al.*, 1999; Helle *et al.*, 2005; Pedersen *et al.*, 2007), and I show how to include them in PIMC by adding a Berry's phase (Berry, 1984) term.

The mapping from a continuous model with interacting particles to a lattice model introduces subtle complications. For a non-interacting system it is reasonable to reduce the Hilbert space to just one orbital per site, coupled by a hopping matrix element, t. The non-interacting many-body ground state is a product state of these single particle orbitals. Low-energy excited states are spanned by this basis, so an effective lattice model is an excellent approximation. Interactions are typically added to this lattice model as on-site energies, U, or intersite terms, V. For small t, this gives the well-known $J = 4t^2/(U - V)$.

There can be a serious flaw when considering interactions in this order. When interactions are added to the continuum Hamiltonian, correlation enters as virtual excitations to higher energy orbitals. At first this seems insignificant, since there may be still a one-to-one mapping to an effective lattice model. But, when choosing effective lattice parameters, one must remember that many-body states in the continuum model have quantum fluctuations that are simply not present in the lattice model.

3.2 Modeling and Method

As a specific example, consider two electrons in a double quantum dot. This system is often represented as a two-site Hubbard model, where the sites represent the $1s$ ground states of the dots. Correlation terms involve virtual excitation of the electron to the $2p_x$ and $2p_y$ states of the dots. These quantum fluctuations generate van der Waals attraction, in addition to mean-field repulsion. Van der Waals attraction and other correlations renormalize the interaction parameters to new values, U_r and V_r.

When I consider hopping between sites, more complications emerge. The hopping barrier has contributions from both the external potential and electron-electron interactions. While the mean-field Hartree contribution can simply be added to the effective potential, the fluctuating part is not so trivial. In the transition state, an electron passes over a barrier whose height has quantum fluctuations. Thus I expect interactions to renormalize the hopping constant, t_r. At the Hartree-Fock level, Hund-Mulliken theory already predicts a renormalized t_r and U_r due to long-range exchange (Mattis, 1981; Burkard *et al.*, 1999). However,

neglect of correlation in Hund-Mulliken theory can lead to catastrophic failure at intermediate dot separations (Pedersen *et al.*, 2007). PIMC includes all correlations, and illuminates their role in barrier hopping with the concept of instantons.

I start with the two-dimensional model for the GaAs double quantum dot studied in Pedersen *et al.* (2007),

$$H = \frac{\mathbf{p}_1^2}{2m^*} + \frac{\mathbf{p}_2^2}{2m^*} + \frac{e^2}{\epsilon|\mathbf{r}_1 - \mathbf{r}_2|} + V_{\text{ext}}(\mathbf{r}_1) + V_{\text{ext}}(\mathbf{r}_2), \tag{3.1}$$

with $m^* = 0.067m_e$ and $\epsilon = 12.9$. The external potential comes from two piecewise-connected parabolic potentials,

$$V_{\text{ext}}(\mathbf{r}) = \tfrac{1}{2}m\omega_0\{\min[(x-d)^2, (x+d)^2] + y^2\}, \tag{3.2}$$

with minima at $x = \pm d$. I report d relative to the oscillator length $r_0 = \sqrt{\hbar/m\omega_0}$. The two lowest energy two-electron states are spatially symmetric and anti-symmetric under exchange, with energies ε_+ and ε_-, respectively. The exchange coupling, $J = \varepsilon_- - \varepsilon_+$, has been calculated previously using direct diagonalization on a basis of Fock states built from seven single particles states (Pedersen *et al.*, 2007). Much care was taken to test convergence with the number of states and careful evaluation of Coulomb matrix elements. I note that the same quality of direct diagonalization calculation in three dimensions would typically take more single particle states.

QMC techniques give essentially exact answers to many problems without basis set convergence issues, and often work just as easily in multiple dimensions. PIMC is nice for quantum dot problems (Harowitz *et al.*, 2005) because it does not require a trial wavefunction. However,

direct calculation of either ε_+ or ε_- with PIMC often have large statistical errors in energy (~ 1 meV in dots). Instead, I use particle exchange statistics to estimate energy differences J to high accuracy (~ 1 μeV) in PIMC.

To calculate J, I split the partition function into terms that are spatially symmetric and antisymmetric under exchange, $Z = Z_+ + Z_-$. These terms can be expressed as symmetrized or antisymmetrized imaginary-time path integrals (Feynman, 1972; Ceperley, 1995)., (see E),

$$Z_\pm = \frac{1}{2!} \sum_{P=\mathcal{I},\mathcal{P}} (\pm 1)^P \int \mathcal{D}R(\tau) e^{-\frac{1}{\hbar} S_E[R(\tau)]}. \tag{3.3}$$

This is a sum over all two-particle paths $R(\tau)$ with the boundary condition $R(\beta\hbar) = PR(0)$, ($P = \mathcal{I}, \mathcal{P}$), where $\mathcal{P}$ swaps particle positions and $\mathcal{I}$ is the identity. The symbol $(\pm 1)^P$ takes the values $(\pm 1)^{\mathcal{I}} = 1$ and $(\pm 1)^{\mathcal{P}} = \pm 1$. At low temperature, only one state contributes to each partition function, so $Z_\pm = e^{-\beta\varepsilon_\pm}$. Thus,

$$e^{-\beta J} = \frac{Z_-}{Z_+} = \frac{\sum_P \int \mathcal{D}R\, (-1)^P e^{-\frac{S_E}{\hbar}}}{\sum_P \int \mathcal{D}R\, e^{-\frac{S_E}{\hbar}}} \equiv \langle (-1)^P \rangle_+, \tag{3.4}$$

or $J = -k_B T \ln\langle (-1)^P \rangle_+$. Thus the exchange coupling can be calculated by sampling a symmetric (bosonic) path integral (Ceperley, 1995) and taking the average of $(-1)^P$, which is $+1$ for identity paths and -1 for exchanging paths.

3.3 Results

I ran PIMC simulations (Ceperley, 1995) with my open-source pi code for the dots studied in Pedersen *et al.* (2007), with the results shown in Fig. 3.1 (a). Coulomb interactions are included with a pair action that correctly handles the cusp condition. I observed convergence of the

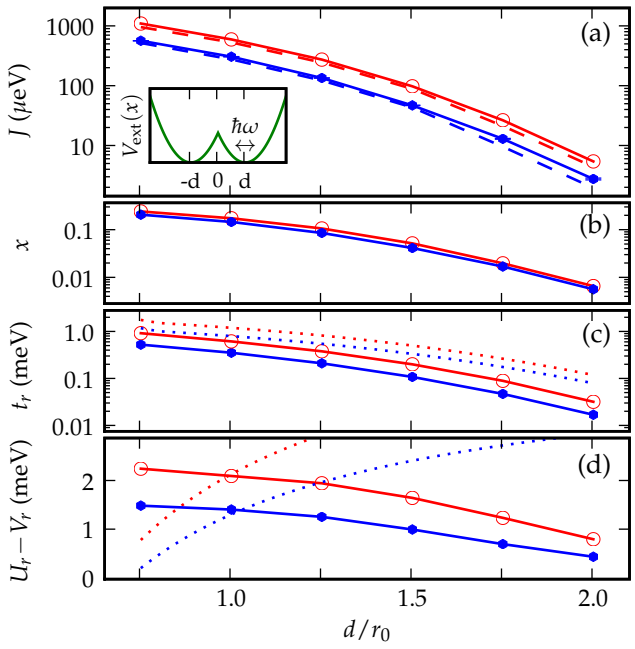

Figure 3.1: PIMC results for double dot. (a) Exchange couplings J for $\hbar\omega = 4$ meV (•) and $\hbar\omega = 6$ meV (○) double dots with a piecewise parabolic potential (inset). Dashed lines are direct diagonalization results from Pedersen *et al.* (2007). (b) The double dot occupation probability x. Using J and x I fit (c) t_r and (d) $U_r - V_r$ parameters for an effective two-site Hubbard model. Dashed lines in (c) show the bare hopping t for one electron in the double dot. Dashed lines in (d) are $V - U$ with $V = e^2/2\epsilon d$ and U taken from a PIMC calculation on a single dot.

path integral results with 6400 discrete slices, but a higher-quality pair action (Ceperley, 1995) could require fewer slices. I see near perfect agreement with DD, and speculate that small deviations may be due to the finite basis in the DD calculation or approximations in the evaluation of Coulomb matrix elements at larger d (Pedersen *et al.*, 2007).

To learn more, I collect the two-particle density, $\rho(x_1, x_2)$, which is the probability to find one electron at x_1 and the other at x_2, integrated over all values of y_1 and y_2, and shown in Fig. 3.2 (b). I calculate double occupation, x_D, which I define as the probability for the electrons to lie

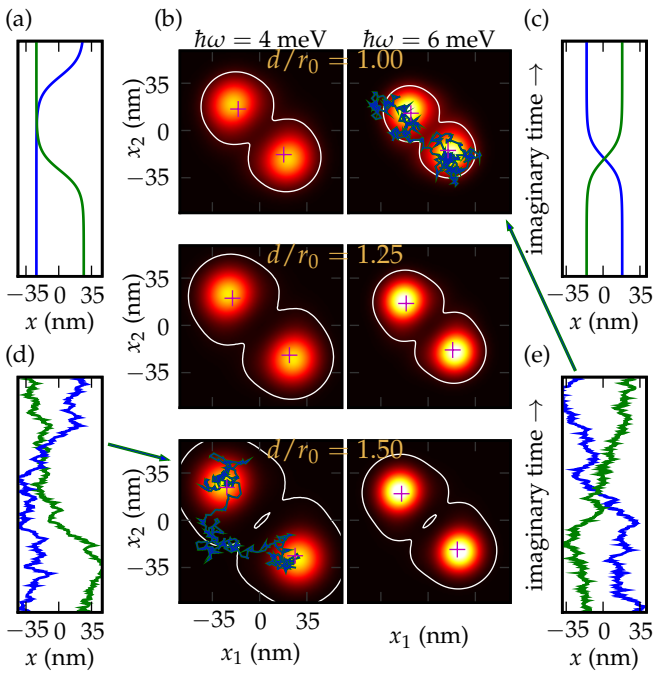

Figure 3.2: Paths and pair densities for a double dot. (a) Simplified instanton with double occupation of the right dot. (b) Pair densities $\rho(x_1, x_2)$ with the lowest density contour line that connects both potential minima (+ markers) at $(\pm d, \mp d)$. (c) Simplified instanton with simultaneous exchange. (d) Actual path showing double occupation, sampled from $\hbar\omega = 4$ meV, $d = 1.5r_0$ dots. (e) Actual path showing simultaneous exchange, sampled from $\hbar\omega = 6$ meV, $d = r_0$ dots. Trajectories (d) and (e) are also plotted in (b).

on the same side of the $x = 0$ plane(double occupation). From J and x_D I use the two-site Hubbard to deduce renormalized values for t_r and $U_r - V_r$, Fig. 3.1 (c) and (d). Detailed calculations are given in Appendix D. Interactions renormalize t_r to smaller values, consistent with Hund-Mulliken theory or a larger renormalized mass. The larger J arises from the dramatic decrease in $U_r - V_r$ at larger dot separations, as correlation enables more virtual hopping.

There are two minima, $(x_1, x_2) = (\pm d, \mp d)$, in the total potential, marked '+' in Fig. 3.2(b). For non-zero J, some paths must go between

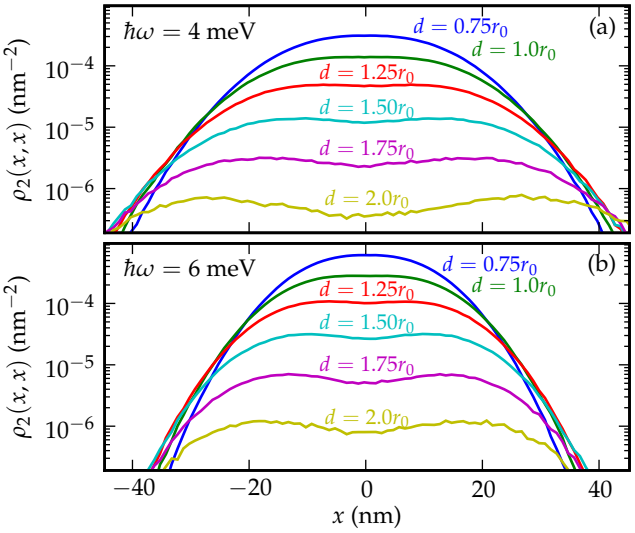

Figure 3.3: Crossing density, $\rho_2(x,x)$, equivalent to the diagonal of the pair densities in Fig. 3.2(b).

these minima. In a semiclassical picture, the paths fluctuate around the potential minima, with rapid crossings called instantons, in which particles exchange between the dots. An instanton can involve brief double-occupation of a dot, illustrated in Fig. 3.2(a), or simultaneous exchange, as in Fig. 3.2(c). Figs. 3.2(d) and (e) show paths from PIMC that resemble the idealized instantons. In Fig. 3.2(b), one instanton moves from the $(d,-d)$ minimum, briefly double-occupies the left dot, $(-d,-d)$, then moves to the $(-d,d)$ minimum, while the other instanton moves directly between the two minima.

Contours of $\rho(x_1,x_2)$, Fig. 3.2(b), reveal a trend with increasing dot separation. For small d the highest probability is directly between the minima (simultaneous exchange), but at larger d the highest probability has two pathways (brief double occupation). Fig. 3.3 shows the probability density for crossing, $\rho(x,x)$. Crossing is most likely in the middle

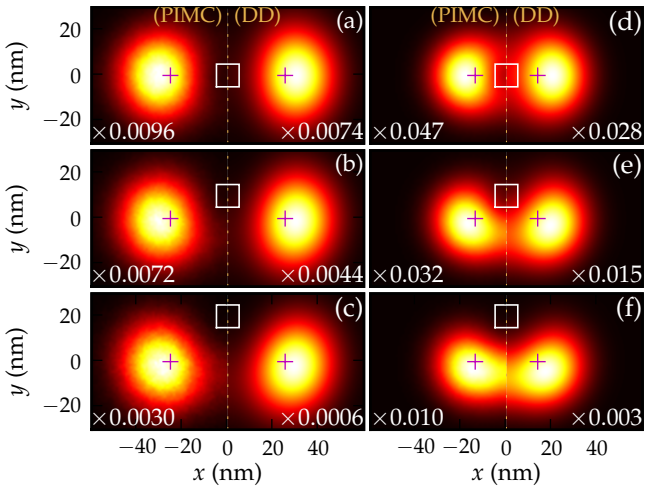

Figure 3.4: Conditional density of one electron when the other electron is in the white box, showing the correlation hole during an instanton. Panels (a)–(c) are the $\hbar\omega = 4$ meV, $d = 1.5r_0$ dots and (d)-(f) are the $\hbar\omega = 6$ meV, $d = 1.0r_0$ dots. Numerical factors are the likelihood of the first electron being in the white box. PIMC results are shown on the left of each image, with direct diagonalization results (Pedersen *et al.*, 2007) on the right.

($x = 0$) when the dots are close together. For larger d, the crossing probability has a double peak near the dots that is about twice the value at $x = 0$. The double peaks are slightly larger for the wider $\hbar\omega = 4$ meV dot, indicating more double occupation.

To underscore the presence of electronic correlation during tunneling, I plot the correlation hole in Fig. 3.4, with PIMC results next to direct diagonalization results (Pedersen *et al.*, 2007). While some quantitative differences are apparent, consistent with the finite basis size in direct diagonalization, the overall agreement is quite good. The message is clear: in the instanton, as one electron moves between the dots, the other electron moves away, enhancing the instanton and increasing J.

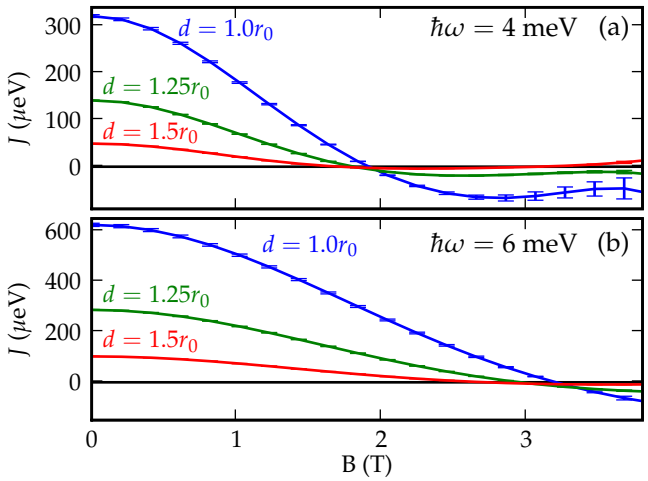

Figure 3.5: Magnetic field dependence included with a Berry's phase for several double quantum dots.

For charged particles, magnetic fields can be used to tune the exchange coupling and even change its sign (Burkard *et al.*, 1999; Harju *et al.*, 2002). In the path integral, a magnetic field is easily implemented as a Berry's phase $q\Phi_B$, where q is the electron charge and Φ_B is the total magnetic flux enclosed by the path of the two electrons. The exchange splitting is then $J(B) = -k_B T \ln(\langle e^{iq\Phi_B}(-1)^P\rangle_+ / \langle e^{iq\Phi_B}\rangle_+)$. The quantities are averaged from the bosonic path integral with no field, so data for different magnetic field strength may be collected simultaneously. For very large magnetic fields the expectation value in the denominator is small and Monte Carlo sampling errors are catastrophic. In practice, I find that fields up to 4 T in strength are practical for the geometries I study, yielding the results in Fig. 3.5.

3.4 Conclusion

In conclusion, I use a simple and elegant method to calculate the exchange energy splitting J from permutations in the bosonic path, which

can also be used in other similar systems. Correlations renormalize t_r and $U_r - V_r$, with a dramatic decrease in $U_r - V_r$ at large separation. I also find that simultaneous paths crossing occurs more often with closely spaced dots, while further separated dots are more likely to have instantons with double occupations. Finally, magnetic field has been applied to confirm the validity of the algorithm.

Chapter 4

STARK EFFECT IN QUANTUM DOTS

In this chapter, I present my results obtained from path integral simulations for excitonic complexes in various kinds of InGaAs quantum dot samples. Since the photoluminescence spectra has been studied extensively for an axial electric field I will first present my results for axial fields on smaller pyramid dots and compare with the existing experimental results (Finley *et al.*, 2004). I next discuss the effect of polarizability (Seafert *et al.*, 2001) and hyperpolarizabilities in the energy shift in the axial growth direction. Then the effect of latera electric field (Heller *et al.*, 1998) on these dots will be discussed. Finally I present results for a larger size lens-shaped, In-rich quantum dot to investigate the effect of dot geometry (Moison *et al.*, 1993; Widmann *et al.*, 1998; Tablero, 2009), size, and In-concentration on photoluminescence spectra.

The energy of a quantum state in a uniform electric field can be expanded as a power series in the field strength, $\boldsymbol{\mathcal{E}}$,

$$\begin{aligned} E(\boldsymbol{\mathcal{E}}) = E_0 - \Gamma^{(1)}_{\alpha}\mathcal{E}_\alpha - \frac{1}{2!}\Gamma^{(2)}_{\alpha\beta}\mathcal{E}_\alpha\mathcal{E}_\beta - \frac{1}{3!}\Gamma^{(3)}_{\alpha\beta\gamma}\mathcal{E}_\alpha\mathcal{E}_\beta\mathcal{E}_\gamma \\ - \frac{1}{4!}\Gamma^{(4)}_{\alpha\beta\gamma\delta}\mathcal{E}_\alpha\mathcal{E}_\beta\mathcal{E}_\gamma\mathcal{E}_\delta - \ldots, \end{aligned} \tag{4.1}$$

where the indices are summed over x, y, and z. Since the dipole moment couples linearly to the applied field,

$$\begin{aligned} d_\alpha(\boldsymbol{\mathcal{E}}) \equiv -\frac{dE}{d\boldsymbol{\mathcal{E}}_{\boldsymbol{\alpha}}} = \Gamma^{(1)}_{\alpha} + \Gamma^{(2)}_{\alpha\beta}\mathcal{E}_\beta + \frac{1}{2!}\Gamma^{(3)}_{\alpha\beta\gamma}\mathcal{E}_\beta\mathcal{E}_\gamma \\ + \frac{1}{3!}\Gamma^{(4)}_{\alpha\beta\gamma\delta}\mathcal{E}_\beta\mathcal{E}_\gamma\mathcal{E}_\delta + \ldots. \end{aligned} \tag{4.2}$$

Thus $\Gamma^{(1)}$ is the zero-field electric dipole moment, $\boldsymbol{d}_0$, and $\Gamma^{(2)}$ is the static polarizability.

4.1 Introduction

In previous papers, calculations on Stark shift energies and other properties of excitons and biexcitons in quantum dots were made (Warburton and Schulhauser, 2002; Sabathil *et al.*, 2003; Pokutnyi and Jacak, 2004). An eight-band $k \cdot p$ Hamiltonian was used to study the anomalous quantum confined Stark effect in vertically stacked InAs/GaAs self-assembled quantum dots. This showed that the anomalous effect is caused by the stain-field distribution (Sheng and Leburton, 2002). An effective-mass envelope function model was also used to calculate the electron and hole energy levels and optical transition energies (Li and Chang, 2005; Wang and Djie, 2006). The relation of exciton and biexciton binding to the vertical Stark effect in a quantum dot were studied with the configuration interaction method using analytical expressions for the single particle wavefunction. Those calculations showed that a weak optical transition is enhanced by the vertical electric field (Tomić and Vukmirović, 2009; Cornet *et al.*, 2005; Korkusinski and Reimer, 2009). The effect of biexciton binding on the Stark effect in GaAs quantum dots has also been investigated using a time-dependent perturbation technique, which showed that the red shift that usually occurs in quantum dot energy levels changes to a blue shift in the presence of biexcitons (Banerjee and Shore, 2005). In all these previous works, the correlation of excitons and biexcitons are handled in an approximate method. In

the PIMC method, I can include all the correlation effects, which gives a more accurate result.

4.2 Methods

Method of generating InGaAs/GaAs self-assembled dot profile

Before running the PIMC simulations, I first generated the models for the self-assembled quantum dots. The effective mass model of a self-assembled quantum dot were made using the following procedure; codes and files for each step are listed in Appendix **??**. Based on experimental information, I design a model for my quantum dot structure that include the shape, size, and composition of the dot and any wetting layer. Next, I relaxed the atomic positions. I used a ball-and-spring model, the valence force field (VFF) model, to calculate the strain energy. I relaxed the atomic positions using conjugate gradients until the maximum force between atoms was less than 10^{-6} atomic units. Finally, I calculated the strain-modified band offsets. In Fig. 4.1, I show a calculated strained band structure of one of my simulated quantum dots after the procedure above.

Effective-mass modeling of quantum dots

To simulate InGaAs nanostructures I assume that the conduction band electrons and valence band holes can be described by a single-band effective mass model,

$$H = \sum_{i=1}^{N_e} \frac{p_i^2}{2m_e^*} + \sum_{i=1}^{N_h} \frac{p_i^2}{2m_h^*} + \sum_{i=1}^{N_e} V_e(\mathbf{r}_i) + \sum_{i=1}^{N_h} V_h(\mathbf{r}_i) + \sum_{i<j} \frac{q_i q_j}{\epsilon r_{ij}} \tag{4.3}$$

where N_e and N_h are the numbers of electrons and holes, m_e^* and m_h^* are the effective masses of dressed electrons and holes, $q = \mp e$ are their

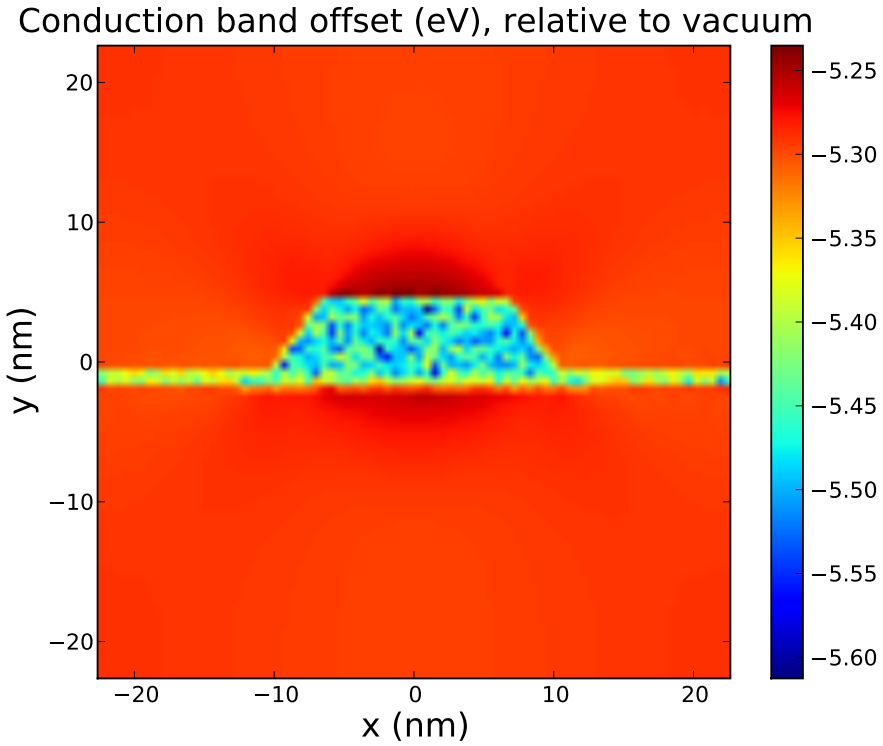

Figure 4.1: Conduction band offset for a uniform self-assembled dot in my simulation

respective charges, and $V_e(\mathbf{r})$ and $V_h(\mathbf{r})$ the effective external potentials arising from band offset (due to composition changes and strain fields) between InAs and GaAs band edges. The last term in Eq. (4.3) represents the interaction between these dressed electrons and holes. Since the nano-structures are composed of different materials I expect the dielectric constant to be spatial varying, but to simplify the PIMC calculations I approximate it by the dielectric constant of GaAs ($\epsilon = 12.5$) everywhere. The effective mass of the electron is taken to be that of conduction band electrons, $m_e^* = 0.067 m_e$, in GaAs. Since the hole mobilities

are different in the growth and transverse directions, I used anisotropic hole effective masses: $m^*_{h,\parallel} = 0.38m_e$ and $m^*_{h,\perp} = 0.11m_e$.

Method of getting spectra

With PIMC I can use two methods to obtain the spectra. First I can apply an electric field directly on my dots, get the energy of exciton and biexciton states in the electric field, and thus determine the PL energies of the exciton and biexciton. The other method is perturbative response theory, which I describe in Appendix B. I simulated six different states—1e, 1h, 1e1h, 1e2h, 2e1h, and 2e2h—in the quantum dots to obtain: the total energy E_0, zero-field dipole moment d_0, the polarizability α, and the hyperpolarizabilities β and γ. Details about how I get the polarizability and hyperpolarizabilities of the system are provided in Appendix B. The photoluminescence transition energies are then,

$$E_X(\mathcal{E}) = E_{1e1h}(\mathcal{E}) \tag{4.4a}$$

$$E_{X^-}(\mathcal{E}) = E_{2e1h}(\mathcal{E}) - E_{1e}(\mathcal{E}) \tag{4.4b}$$

$$E_{X^+}(\mathcal{E}) = E_{1e2h}(\mathcal{E}) - E_{1h}(\mathcal{E}) \tag{4.4c}$$

$$E_{XX}(\mathcal{E}) = E_{2e2h}(\mathcal{E}) - E_{1e1h}(\mathcal{E}) \tag{4.4d}$$

From the equation above, I can also get the PL spectra of the exciton (X), biexciton (XX) and the charged excitons (X^+,X^-). The first method—explicit inclusion of an electric field—gives more accurate results for the energies than the second one, because the second method is perturbative. The direct calculation method has the disadvantage that it cannot give the relative contribution of the polarizability and hyperpolarizabil-

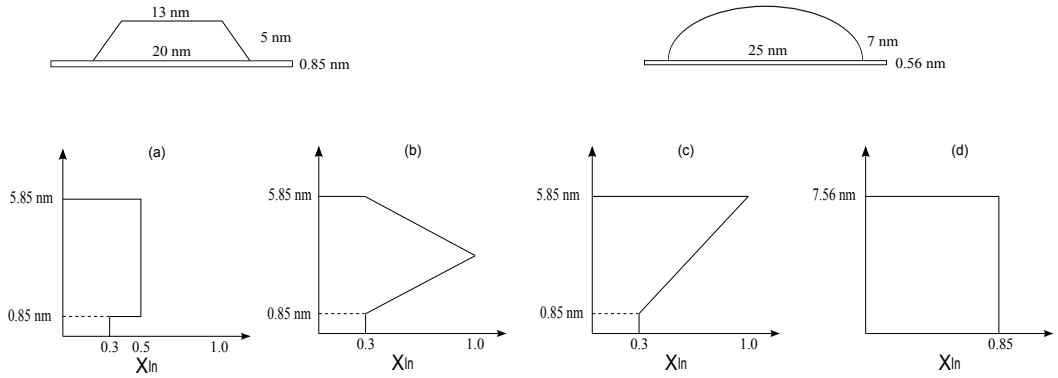

Figure 4.2: Sketches of In_xGaAs quantum dot geometries and their In composition profiles. Simulation done for three varities of truncated pyramid shaped quantum dots uniform (a), peaked (b), graded (c) and one larger lens shaped uniform dot (d).

ities of the state. In this chapter, I use both methods to calculate the PL energies for all different cases.

Three dimensional dot models

As mentioned above, I simulated three varieties of truncated pyramid shaped InGaAs quantum dots; namely, uniform, peaked and graded, and also one uniform lens-shaped dot (Harowitz *et al.*, 2005). In Fig. 4.2 I give the composition (Sabathil *et al.*, 2003) of each dot. For periodic boundary condition one wants to use a supercell that is as big as possible, but this is limited by computation time. I chose it to be $45\times45\times45$ nm^3, so that it is more than twice the diameter of the dot.

The uniform dot sits on a three monolayers of $In_{0.3}Ga_{0.7}As$ alloy with thickness 0.85 nm. The dot is approximately 5 nm tall and 20 nm wide. For uniform composition it is made up with a random alloy $In_{0.5}Ga_{0.5}As$ all throughout. Fig. 4.2(a) shows its geometry and In composition profile.

The supercell is chosen such a way that the dot sits in the middle of the cell, and the rest of the cell is filled with binary alloy GaAs.

Like the uniform dot, the peaked one also sits on three monolayers of $In_{0.3}Ga_{0.7}As$ alloy of same thickness. It also has same dimensions as a uniform dot. But as the name suggests, it is not uniformly composed. Instead, the middle portion is much richer (100% In) in In than the edges (30% In). Fig. 4.2(b) shows the geometry and In composition profile of the dots. Once again rest of the supercell is filled binary alloy GaAs.

Like its other two variants, the graded dot too has the same dimensions and sits on the same kind of wetting layer, but the In density increases linearly with the height. It starts with 30% at the bottom and smoothly increases to 100% at the top. Again, the rest of the supercell is made of GaAs. Fig. 4.2(c) shows its composition profile.

Finally, I also considered a larger, lens-shaped dot. The lens-shaped, uniform dot has a different composition, $In_{0.85}Ga_{0.15}As$, which is shown in Fig. 4.2(d).

I also simulated excitons and biexcitons in a parabolic quantum dot with an electric field. I use a two dimensional simple harmonic oscillator (2D SHO) model,

$$\begin{aligned} H = & \sum_{i=1}^{N_e} \frac{p_i^2}{2m_e^*} + \sum_{i=1}^{N_h} \frac{p_i^2}{2m_h^*} - \frac{1}{2m_e^*}\left(\frac{eE}{\omega_e}\right)^2 \\ & + \sum_{i=1}^{N_e} \frac{1}{2} m_e^* \omega_e^2 \left[\left(x - \frac{eE}{m_e^* \omega_e^2}\right)^2 + y^2\right] - \frac{1}{2m_h^*}\left(\frac{eE}{\omega_h}\right)^2 \\ & + \sum_{i=1}^{N_h} \frac{1}{2} m_h^* \omega_h^2 \left[\left(x + \frac{eE}{m_h^* \omega_h^2}\right)^2 + y^2\right] + \sum_{i<j} \frac{q_i q_j}{\epsilon r_{ij}}. \end{aligned} \tag{4.5}$$

In order to compare the result with Korkusinski and Reimer (2009), I used the same constant value T=12 K, $\epsilon = 12.4$, $m_e^* = 0.055 m_0$, $m_h^* = 0.11 m_0$, $\hbar\omega_e = 12$ meV, and $\hbar\omega_h = 6$ meV.

4.3 Results

In this section I present my results and analysis from path integral simulations for excitonic complexes in a parabolic quantum dot and various kinds of InGaAs quantum dot samples. The results will be presented in the following order. At first I will give the spectra of exciton and biexciton in a parabolic quantum dot and compare the results with those from Korkusinski and Reimer (2009), to show that my method has an advantage in these calculations and will give more accurate results. Secondly, since the PL spectra has been studied extensively for axial electric fields, I shall present my results for axial field on smaller pyramid dots and compare with the existing experimental results (Finley *et al.*, 2004).

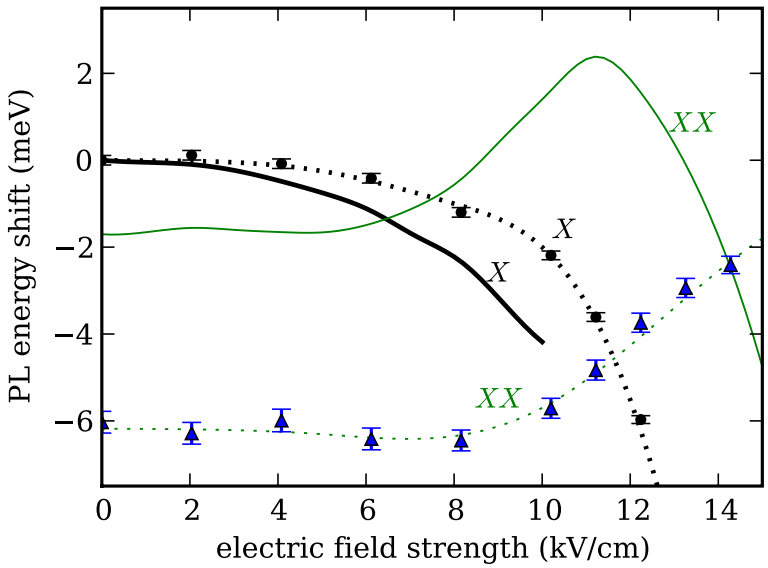

Figure 4.3: Photoluminescence energy shifts for exciton X and biexciton XX in a parabolic quantum dot ($\hbar\omega_e = 12$ meV, and $\hbar\omega_h = 6$ meV), versus lateral electric field. Solid lines are results of CI calculation from Korkusinski and Reimer (2009), which use an under-converged basis constructed from ten non-interacting single-particle states: thick black line is X and thin green line is XX. Data points with error bars are results of PIMC calculations which include all correlation effects: black circles are X and blue triangles are XX. Dotted lines are guide to the eye.

I shall also discuss the effect of polarizability (Seafert *et al.*, 2001) and hyperpolarizabilities in the energy shift in axial growth direction. Then the effect of lateral field (Heller *et al.*, 1998) on these dots will be discussed. Thirdly, I shall study my results for a larger size lens shaped In rich quantum dots to investigate the effect of dot geometry (Moison *et al.*, 1993; Widmann *et al.*, 1998) size, and In concentration on PL spectra. Finally I will add the piezo-electric field to the dot, and analyze how the piezo-electric potential affects the anisotropy of the dots.

Parabolic quantum dot

As I mentioned in the methods section, I use the 2D SHO potential to simulate the exciton and biexciton in a parabolic quantum dot with different lateral electric field. I simulate the electric fields from 0 to 14 kV/cm at every 2 kV/cm. I find the energy of exciton and biexciton state in these fields and calculate the spectra shown in Fig. 4.3. From the graph I see that the energy difference between exciton and biexciton in my calculation is larger than that in Korkusinski and Reimer (2009). The second important difference is the position of the crossing of two spectra, which is an important region for its possibility to discern the electron-hole exchange splitting. This crossing region will be appear at a larger field in my calculation. Finally I find that the curvature of the Korkusinski and Reimer (2009) exciton curve is larger than ours, which means they have larger polarizabilities. This is because Korkusinski and Reimer (2009) use single particle states to construct the many-particle configuration, and lose some of the correlation effects in their results, which makes the exciton easier to ionize. With PIMC I can simulate the exact exciton and biexciton state in the 2D SHO model, which includes all the correlation and gives a more accurate result.

Effect of composition on polarizability

In Fig. 4.4, correlation energies of the excitonic complexes are plotted as a function of axial electric field, which can be directly compared with the experiment. These curves represent the shift (Sanguinetti *et al.*, 2000) (Stark-shift) of the PL (Finley *et al.*, 2001; Reimer *et al.*, 2008) energy peak positions as the field strength is varied. For graded dot,

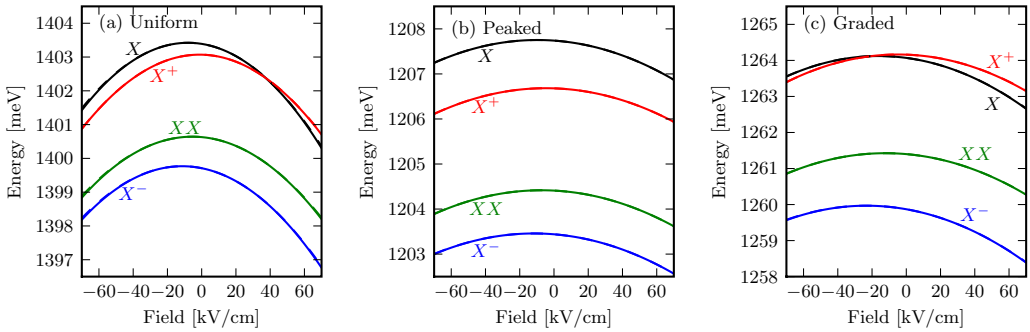

Figure 4.4: PL energies of the excitonic complexes in pyramid shaped uniform (a), peaked (b), graded (c) In_xGaAs quantum dots for axial fields. Here the parabolic fit (broken line) coincides with PL energies (solid line) which means hyperpolarizability effects are minimal.

comparing experimental (Fig. 1(c) of Finley *et al.* (2004)) Fig. 4.5 and theoretical (Fig. 4.4(b)) PL spectra I observe that ΔE between X^- and X^0 is ~ 5 meV; also ΔE between XX and X^0 is $\sim 3 - 2.5$ meV matches very well with the experiment. Though the matching of numbers (ΔE) are very good, the interpretation of the excitonic peaks (e.g. X^0, X^+) in some experimental papers (e.g. Finley *et al.* (2004)) are very different from ours. From figure (2a) and (2b) the ~ 5 meV ΔE match between X^- and X^0 can also be noticed for uniform and peaked dot. Observing the PL spectra I also get a clear order of stability among excitonic complexes i.e X^0/X^+ has more binding energy than XX than X^-. I also notice that my zero field dipole moments vary from 0.017 nm to 0.084 nm, which are one order of magnitude smaller than the experimental observation. But observing the peak positions of the PL (Fig. 4.4) spectra suggests, in all the cases, intrinsic dipole moments (Fry *et al.*, 1999a,b; Barker and O'Reilly, 2000) are along the growth direction regardless of In composition profile which means the electron mainly sits near the bottom of the

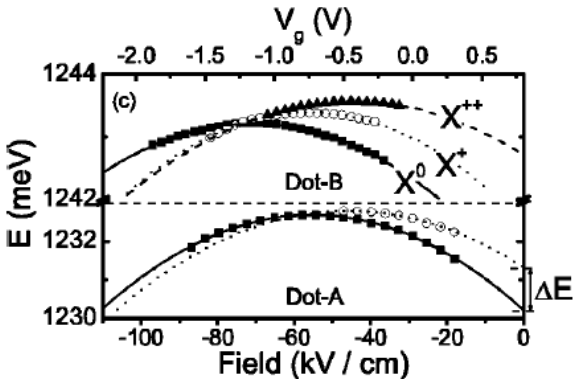

Figure 4.5: The X^0 and X^+ energy as a function of applied field in experiment from Finley *et al.* (2004)

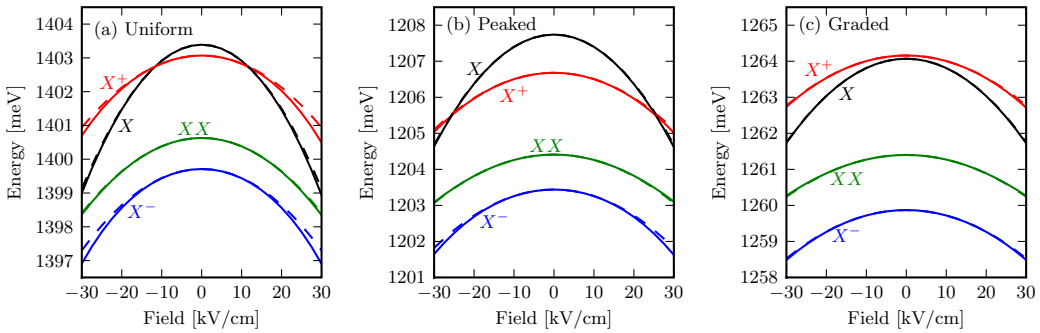

Figure 4.6: PL energies of the excitonic complexes in pyramid shaped uniform (a), peaked (b), graded (c) In_xGaAs quantum dots for transverse fields. Here the parabolic fit (broken line) some times deviates from PL energies (solid lines) which means hyperpolarizability effects may not be neglected.

dot where as holes stay near the top. I also observe for the graded dot polarizability $\alpha_z \sim 40$ e.nm^2/V which matches with the experimental value (Fig. 2(b) of Finley *et al.* (2004)) remarkably well. Polarizability values for the other dots are also very similar. My simulation suggests that higher order hyperpolarizability contributions to PL spectra are negligible in the growth direction.

It is important to investigate excitonic properties in the transverse direction because of symmetry and the larger spatial/geometrical extent. I tabulated the theoretical prediction of polarizabilities and hyperpolarizabilities and show the PL spectra in transverse direction in Fig. 4.6. As expected the PL spectra in the transverse direction is symmetrical about zero field. Due to symmetry, intrinsic dipole moments do not contribute to the energy shift, and $\beta_x \sim 0$, as can be inferred from Appendix C. Due to larger lateral extent, the transverse polarizability α_x and hyperpolarizability γ_x are almost one to two orders of magnitude greater than those in growth direction. This is clearly visible when I compare Fig. 4.4 and 4.6, as the real data deviates from parabolic fit much more in transverse direction than the growth direction even when maximum applied field is only about half of that applied in growth direction. So far the binding energy of the excitonic complexes are concerned the relative order does not change as much as that in growth direction. Once again ΔE between X^- and X^0 is maximum, around 5 meV for all three dots.

Next I study the lens-shaped dot (Mui *et al.*, 1995) which is bigger in size and much more In rich than pyramid-shaped dots discussed earlier. It sits on a two monolayers of $In_{0.85}Ga_{0.15}As$ alloy of thickness 0.56 nm. Its diameter is $\sim$ 25 nm and height is $\sim$ 5 nm. It is uniformly composed of the same alloy $In_{0.85}Ga_{0.15}As$. Since the dot is bigger, one needs to use larger supercell to use periodic boundary condition correctly. My supercell size is $\sim 54\times54\times54$ nm^3, almost 20% bigger than previous simulations. The cell is chosen such a way that the dot sits at the center. As usual it is filled with uniform GaAs. Fig. 4.2(d) shows its geometry and In composition profile.

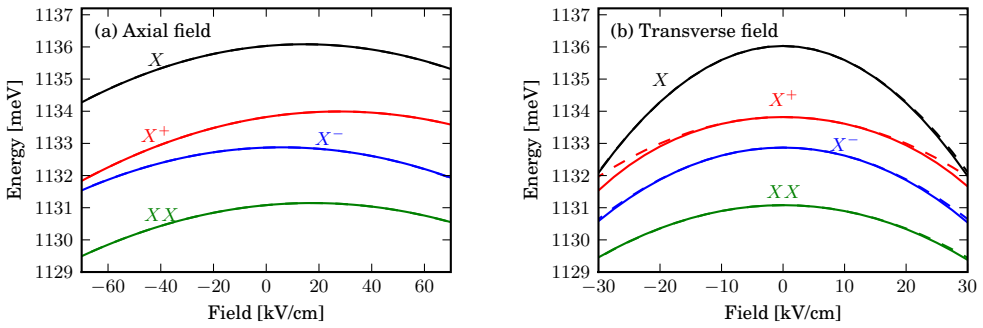

Figure 4.7: PL energies of the excitonic complexes in lens shaped In_xGaAs quantum dots for axial (a) and transverse (b) fields. For axial field the parabolic fits (broken line) exactly coincides with PL energies (solid lines) which means hyperpolarizability effects can be neglected where as for transverse field the parabolic fits (broken line) deviates most from PL energies (solid lines) among all dots suggesting that hyperpolarizability effects are strong and should not be neglected.

The photoluminescence spectrum for lens shaped dot is given in Fig. 4.7. For an applied axial field, Fig. 4.7(a), the first thing to notice is that the peak appears on the other side of zero, in contrast to the pyramid dots, suggesting the opposite distribution of electron and hole. This observation is important as some recent experiments show (Fry *et al.*, 1999a) a change of intrinsic dipole moment sign with the change of quantum dot geometry. Also notice the change of binding energies of excitonic systems in compare to the pyramid dots. Unlike X^- in pyramids here the XX is least stable, though X^0 is still the most stable and ΔE between them is once again about 5 meV. The hyperpolarizability contribution is negligible here too.

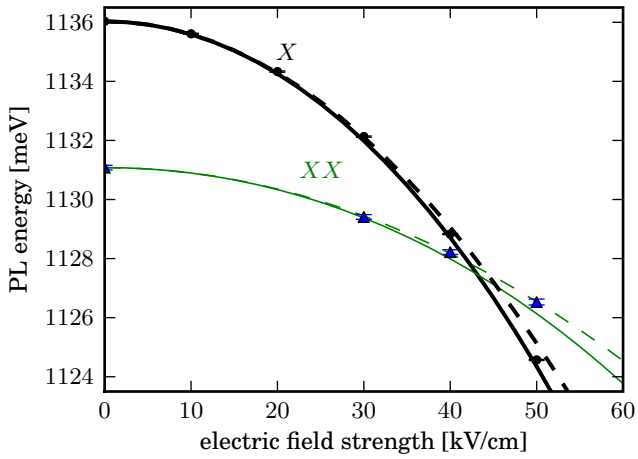

Figure 4.8: PL energies of exciton and biexciton in lens shaped quantum dot for lateral fields, broken line for parabolic fit and solid line for higher order fit. Data points with error bars are results of PIMC calculation of exciton and biexciton in different electric fields.

The lateral field photoluminescence spectrum is shown in Fig. 4.7(b). Due to the symmetry one expects the intrinsic dipole moment and β_x to be zero so that the photoluminescence spectra is symmetric about zero field, which is clearly reflected in the graph. The important thing to notice again is the prominence of hyperpolarizability terms as can be seen in Appendix C.

Crossing of X and XX energies in lens shaped dot

I used PIMC to calculate the exciton and biexciton in several different electric fields to confirm my hyperpolarizability fitting method. I found that the direct calculated energy is very closed to my fitting curve. In Fig. 4.8, I show an increased range of the electric field from 30 kV/cm to 60 kV/cm in order to find the crossing area of exciton and biexciton in my lens shaped quantum dot. I find that the crossing area in my dot is

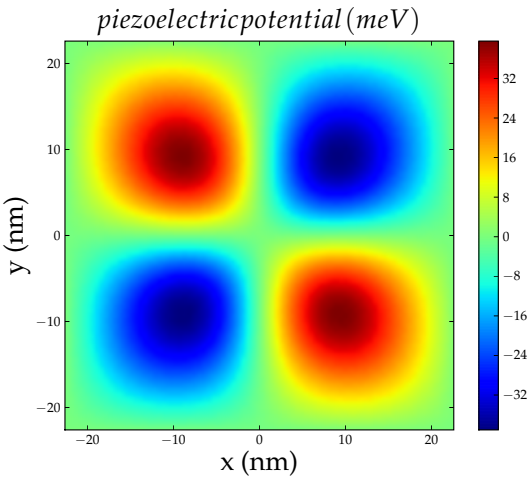

Figure 4.9: This is a top view piezoelectric potential graph of x-y plane just above the uniform dot. From the graph I can see the distribution of positive and negative piezoelectric potential above the dot. Below the dot, the sign of the piezoelectric potential is reversed.

at an electric field of 42 kV/cm, much larger than that in Fig. 4.3. This is because my quantum dot has much larger confinement ($\hbar\omega_e = 46$ meV, and $\hbar\omega_h = 26$ meV) than that dot, which makes exciton and biexciton hard to be polarized.

Effect of piezoelectric field

In the simulation above, I did not include the piezoelectric field in the confinement of quantum dot. In this section I consider this effect. First I generated a piezoelectric potential, Fig. 4.9, from the strain composition of my dot. After I added the piezoelectric potential to the simulation, I find that polarizability in $[110]$ is about 20% smaller than that in $[1\bar{1}0]$ direction, which was very close to that without the piezoelectric field. This clearly shows the anisotropic effect in the x-y plane when I add the piezoelectric field. Next I applied an electric field of 50 kV/cm and -50 kV/cm along z-axis. When I applied a field of 50 kV/cm, I found that the

polarizability increased in [110] direction and decrease in [$1\bar{1}0$] direction. This is because the applied field makes the exciton in the dot more likely to be located in the negative region of Fig. 4.9. When I applied the negative field, the difference between the two directions increased, since in this case the exciton is more likely to be localized in the positive region of Fig. 4.9. This effect can be compared and contrasted to the quantum ring simulations by McDonald and Shumway (2010). They showed how the vertical electric field couples to in-plane anisotropy. However the piezoelectric potential inside of a ring, which I do not have in the quantum dot case, affects the exciton polarizability much more strongly than is seen here.

4.4 Conclusion

In conclusion, the PIMC method is used to calculate the energy, dipole moment, polarizability and hyerpolarizability of excitonic systems in four different quantum dot samples for both growth and transverse direction (Figs. 4.4, 4.6, and 4.7). From this I infer that it is possible to change the intrinsic dipole moment direction by changing the dot geometry, as suggested by recent experiments. Another important part of this research is the study of the effect of hyperpolarizability on the photoluminescence spectra. The hyperpolarizability is a higher order term which cannot be ignored in larger lateral dimensions ($\sim$ 23 nm), since it does change the spectra in large E field region. Finally I add the piezoelectric field to the dots and find the relation how vertical electric field cause anisotropy of the lateral polarizability.

Chapter 5

VAN DER WAALS INTERACTIONS BETWEEN DOUBLE QUANTUM WIRES

In this chapter, I use the PIMC method to calculate the van der Waals interaction between two wires with different separations and temperatures, in order to find the relation between them. I simulated 110 electrons in two parallel, long quantum wires whose length is 1100 atomic units radius. I do this simulation in both 2-dimension(quasi 1D) and exact 1-D condition. In the 2-D simulations, I use the parabolic confinement in y direction to make the radius of the wire be about 1 a.u.

5.1 Introduction

Parallel, thin, electrically neutral wires attract each other by van der Waals forces. Recent investigations (Dobson *et al.*, 2006) show that the usual sum of R^{-6} contributions for elements separated by distance R can give qualitatively wrong results for van der Waals interaction between metallic nanowires, nanotubes, and nanolayered systems, which include π-conjugated systems such as graphite, graphitic hydrogen storage systems (Rydberg *et al.*, 2003a; Dion *et al.*, 2004), and graphene planes. In all the case above, using the correlation energy from the random phase approximation (RPA) (Pitarke and Eguiluz, 1998; Furche, 2001; Fuchs and Gonze, 2002; Dobson and Wang, 1999) gives van der Waals interaction falling off with a power of separation different from the naive atomic result. The RPA method (Longe and Bose, 1993) considers the zero-point energy of the delocalized coupled one dimensional plasmon

modes with wave number parallel to the wire axis. From the RPA technique, the frequency of plasmon corresponding to wave number q is,

$$\omega_{\pm}(d) = (2N_0e^2/m_e)^{1/2}|q|||\ln(qb)| \pm K_0(qd)|^{1/2}, \tag{5.1}$$

where d is the distance between two wires, N_0 is the number of electrons in unit length, b is the radius of wires and K_0 is modified Bessel function. The van der Waals energy of two wire with separation d is the sum of zero-point plasmon energies,

$$E^{vdW}(d) = \frac{L}{2\pi}\int_{-\infty}^{\infty}\frac{\hbar}{2}(\omega_+(d) + \omega_-(d) - 2\omega_+(\infty))dq. \tag{5.2}$$

For the case $d \gg b$, this equation can be approximate as,

$$E^{vdW}(d) \approx -\frac{L\hbar(2N_0e^2/m_e)^{1/2}}{16\pi d^2(\ln(2.39d/b))^{3/2}}. \tag{5.3}$$

Quantum Monte Carlo (QMC) methods have previously been used to calculate the binding energies of pairs of thin metallic wires and layers modeled by 1D and 2D homogeneous electron gases with neutralizing backgrounds (Drummond and Needs, 2007). The QMC result are in broad agreement with RPA in 1-D binding energy and complete disagreement with the naive pairwise van der Waals model. Unlike the previously used ground-state QMC method, the PIMC method can be used to calculate the van der Waals interaction between two wires in finite temperature, which can be used to study the temperature dependance of the van der Waals interaction.

5.2 Method

Pair correlation functions and the Van der Waals interaction

With PIMC, I can directly collect the density-density pair correlation function between the electrons in the one wire or two different wires,

from which I can calculate the van der Waals interaction between two neutral wires. I define the density-density pair correlation function as:

$$g(x,x') = \frac{\langle n_i(x) n_j(x') \rangle}{\langle n_i(x) \rangle \langle n_j(x') \rangle}, \tag{5.4}$$

where $n_i(x)$ represent the density of particles at place x. Indices i and j refer to the wire: if $i = j$, I consider the correlation of electrons in one wire; otherwise, I collect the correlation of electrons in different wires. The quantities $\langle n_i(x) \rangle$ and $\langle n_j(x') \rangle$ are just the average density of electrons in the wire, $N/L = 55/1100\,\text{a.u.} = 0.005\,\text{a.u.}^{-1}$ If there is no correlation between electrons at positions x and x' in same or different wires the correlation function will be $g(x,x') = 1$.

Using the pair correlation between wires, the van der Waals interaction between two wires can be written as,

$$U(d) = \frac{e^2}{4\pi\epsilon_0} (\frac{N}{L})^2 \int dx dx' \frac{g(x,x') - 1}{\sqrt{(x-x')^2 + d^2}}. \tag{5.5}$$

In the equation above, the -1 term represent Coulomb interaction between two wires whose electrons are uniformly distributed; it can be also considered as the neutralized background of my wires. When I subtract that term from the total interaction, I obtain the van der Waals interaction between two neutralized wires, which can be treated as a similar system as RPA and QMC simulations. From PIMC, I implemented an estimator to collect $g(x,x')$. Using Eq. (5.5), I add interactions of all pairs of x, x' to obtain total van der Waals interaction as a function of distance d.

As I mentioned above, when I try to calculate the van der Waals interaction, I put a total of 110 electrons in two 1100 a.u. long wires in both

2-D and 1-D conditions. In the 2-D simulations I use parabolic potential confinement in y direction to model two parallel wires along x axis. I use two different species of electrons; each species has 55 electrons. Spin up electrons are confined in parabolic potential centered at $y = \frac{d}{2}$, and spin down electrons in a potential centered at $y = \frac{d}{2}$, where d is the separation between wires. The reason that I do not use double well potential for the confinement is because I want to prevent the electrons of one species from hopping to the other wire. The Hamiltonian of the double wire system in 2-dimension can be written as,

$$H = \sum_{i=1}^{N_e} \frac{p_i^2}{2m_e} + \sum_{i<j} \frac{q_i q_j}{\epsilon r_{ij}} + \sum_{species1} \frac{1}{2} m_e^* \omega_e^2 (y - d/2)^2 + \sum_{species2} \frac{1}{2} m_e^* \omega_e^2 (y + d/2)^2. \tag{5.6}$$

In the 1-D simulation, I did not need to put a confinement potential in y direction. I manually separated the two wires with distance d and also do not allow the electrons to hop between them as in the 2-D case, thus the Hamiltonian is,

$$H = \sum_{i=1}^{N_e} \frac{p_i^2}{2m_e} + \sum_{i<j} \frac{q_i q_j}{\epsilon r_{ij}}. \tag{5.7}$$

Since I want to calculate the van der Waals interaction between two narrow metallic wire and compare my results with the RPA (Dobson *et al.*, 2006) and QMC (Drummond and Needs, 2007) results , I use the constant value, $\epsilon = 1$, and $\hbar\omega_e = 1$ Ha. From a simple calculation I can estimate that the radius of wire is $\sqrt{\frac{\hbar}{m_e \omega_e}} = 1$ a.u. One of the difficult parts in my simulation is the selection of the temperature, since both RPA and QMC results are based on ground state condition, which is at zero temperature. As I mentioned in Chapter 2, PIMC is a finite temperature technique. So I have attempted to lower my temperature to

make sure my results can be compared with RPA and QMC. However, because the efficiency of the simulation will also drop with the temperature, I need to properly choose my temperature value. In my simulation, I tried both case at different temperature, range from $k_BT = 0.005$ Ha to $k_BT = 0.1$ Ha

5.3 Results

In this part I discuss and present my results in following order. At first, I show the electron density of my 2-D simulations, where the density of the total system is collected by averaging the position of each slice on all the paths. Because of the translational symmetry in the wire direction, theoretically I can anticipate that the average density in each wire is uniform. The density profile helps show us if the system has been fully sampled, thus helps gauge the reliability of my simulations. Secondly, I show the density-density pair correlation function between electrons in both the same wire and different wire. This graph gives us a straightforward sense about what pair correlation functions look like, which also help us more clearly to understand the correlation effects between electrons. Correlation in two different wires are directly used to calculate the van der Waals interaction. Then I show the corresponding results for 1-D simulation. Comparing these to the 2-D cases, I investigate the similarity and difference of these two kind of simulations. Finally, I will put the results from RPA and QMC together with my PIMC results, compare the power law $E^{vdW} \propto -d^{-P}$, and discuss the effect of finite temperature.

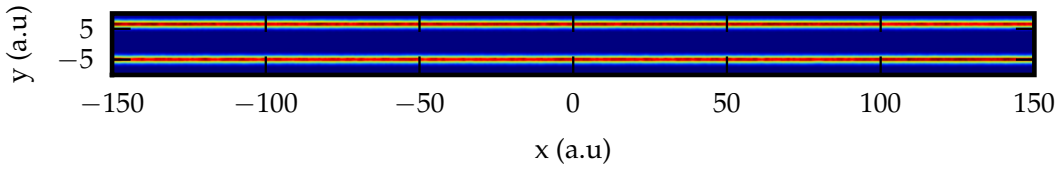

Figure 5.1: The density of two wires when the interwire separation $d = 10$ a.u. and the temperature $kT = 0.1$ Ha. Red part represents higher density of the electron and blue part represent little or no electronic density. Both x-axis and y-axis are in atomic units.

2-D simulation result

As I mentioned in the previous section, I use two SHO potentials to confine the electrons in two wires, and simulate the systems at different temperatures and for different wire separations. By changing the equilibrium position of the parabolic potential, I simulated two wires with separation from 8 a.u. to 20 a.u. I used three temperatures: $k_BT = 0.01, 0.02$ and 0.1 Ha in my simulations. I collected the density from simulation with $d = 10$ a.u. and $kT = 0.1$ Ha as shown in Fig. 5.1. I can see clearly that in the y direction, the electrons are well confined near $y = \pm 5$ a.u., and the width of each wire is fairly small, about 1 a.u. according to my estimation. In the x axis, instead of ploting the total wire, I only plot about 300 a.u long part in the middle of the wire to make the Fig. 5.1 easier to view. From Fig. 5.1, I can see that the red color (representing high electron density) along the wire is quite uniform, although there exist some small difference due to the density fluctuation. Thus I can say that the average electron density in the wires is uniformly distributed, as I predicted theoretically, and from this point of view, the sampling of my simulation is efficient enough to be used to do the calculation.

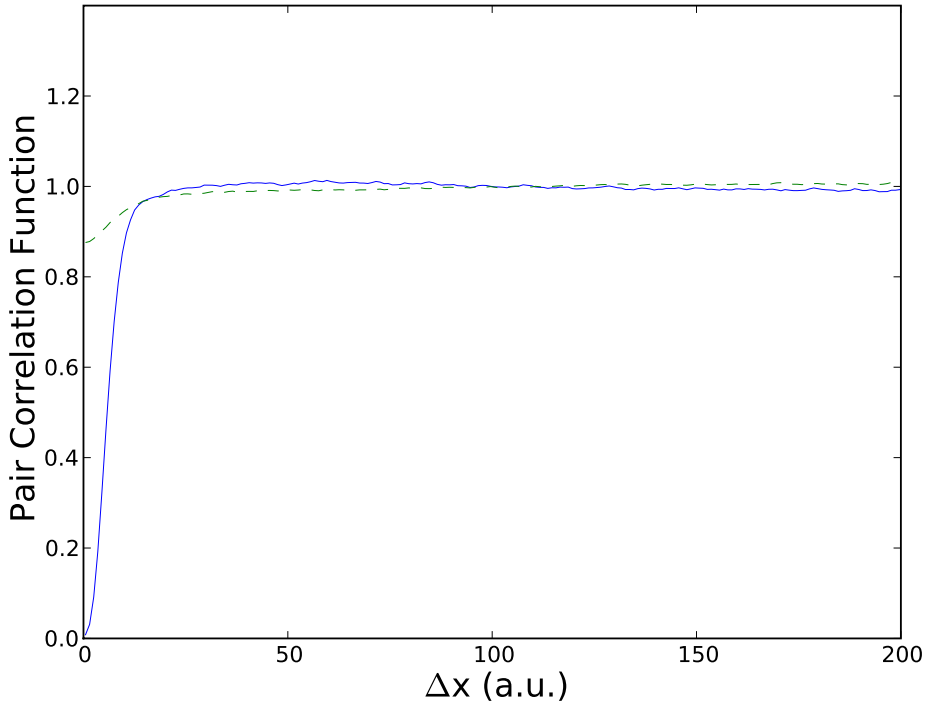

Figure 5.2: This is the density-density pair correlation function for a 2D simulation with wire separation $d = 10$ a.u. and temperature $kT = 0.1$ Ha. The blue line represents the pair correlation of two electrons in same wire and the green one refers to the pair correlation function between different wire

I present three density-density correlation function graphs Fig. 5.2, Fig. 5.3 and Fig. 5.4in different simulation condition. In all these graphs, the y axis show the value of the correlation function

$$g(x, x') = \frac{\langle n_i(x) n_j(x') \rangle}{\langle n_i(x) \rangle \langle n_j(x') \rangle}. \tag{5.8}$$

Due the translational symmetry along wire direction, I find that the pair correlation function is a function of the relative position of two electrons $\Delta x = x - x'$, which is the x-axis of all the graphs. Since I use periodical boundary conditions in my simulation, the super cell size equals

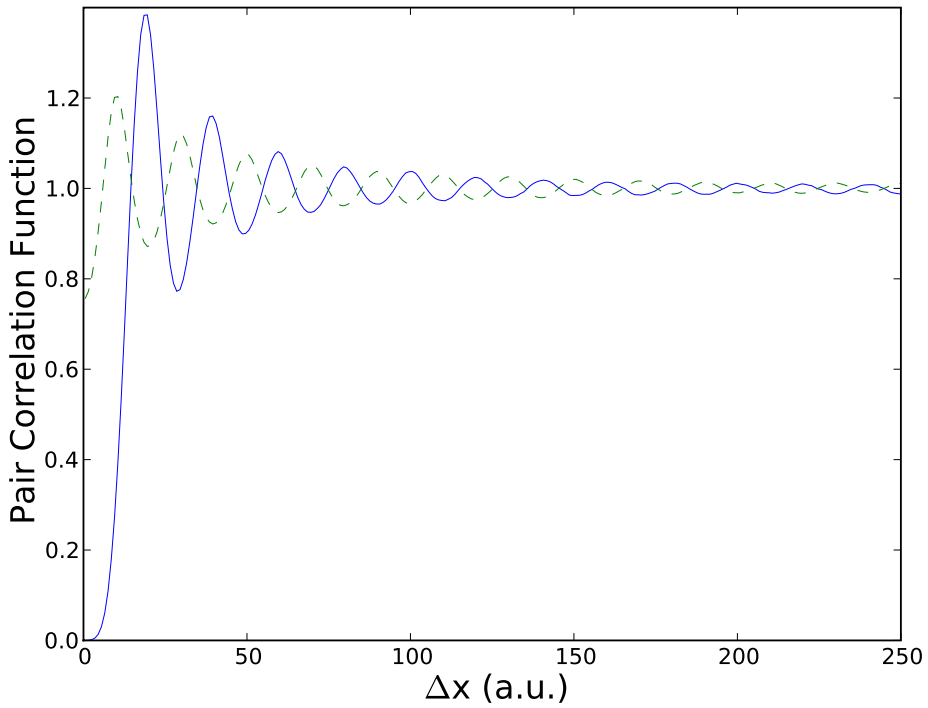

Figure 5.3: This is the density-density pair correlation function in 2D simulation with wire separation $d = 10$ a.u. and temperature $kT = 0.01$ Ha. The blue line represents the pair correlation of two electrons in same wire and the green one refers to the pair correlation function between different wire

to the length of wires (1100 a.u.), the value of $\Delta x = x - x'$ can be set from -550 a.u. to 550 a.u. The pair correlation function equals zero in blue line at $\Delta x = 0$, in all figures. This is because Coulomb interaction and Pauli exclusion prevent two electrons of the same species to be on the exactly same spot. For the pair correlation in different wires, I also see a relative low value at $\Delta x = 0$ position, which shows the Coulomb repulsive interaction also lowers the probability that two electrons are simultaneously at the same x coordinate in different wires. This effect dampens quickly with the increase of wire separation. Another similar

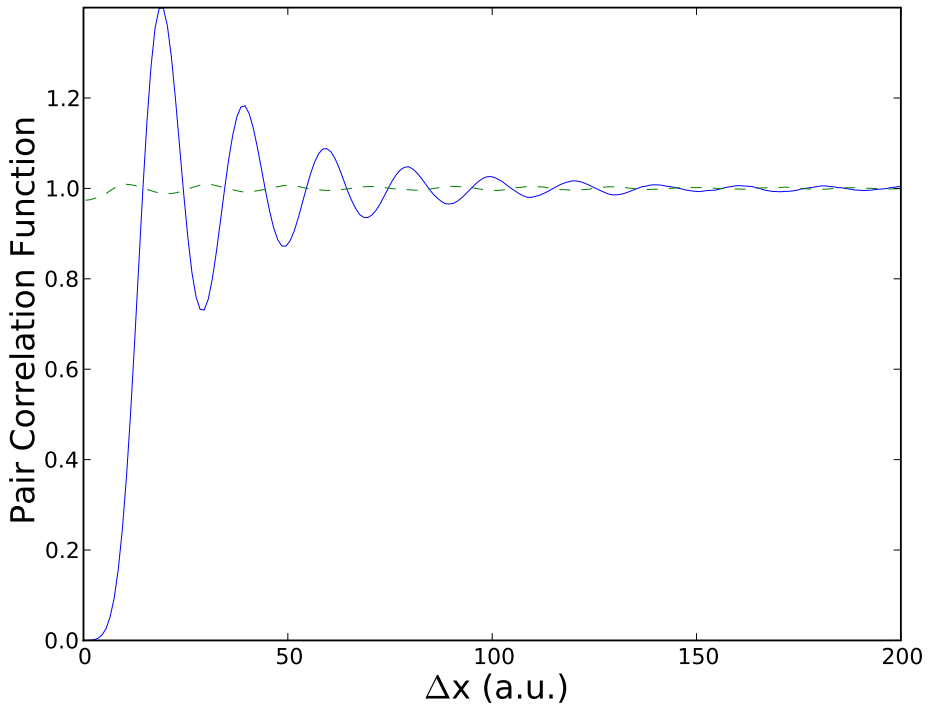

Figure 5.4: This is the density-density pair correlation function in 2D simulation with wire separation $d = 20$ a.u. and temperature $kT = 0.01$ Ha. The blue line represents the pair correlation of two electrons in same wire and the green one refers to the pair correlation function between different wire

things in all three graphs is that when $|\Delta x|$ becomes large (> 200 a.u.), the value of the pair correlation function goes to 1, which means the correlation between electrons with large distance is almost zero. Fig. 5.2 and Fig. 5.3 are density-density pair correlation function with same wire separation and different temperature. I can clearly find the difference between these two Figs. Fig. 5.3 has obviously more oscillations in pair correlation function than that in Fig. 5.2. This is because at low temperature, the effect of Coulomb interaction is more obvious, which makes the correlation between electrons exist at a relative long range. When

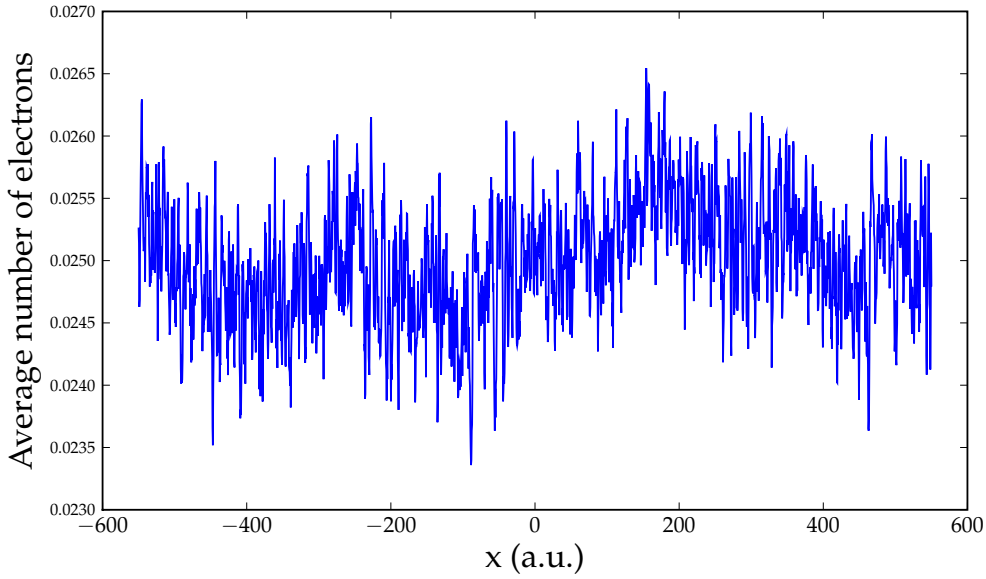

Figure 5.5: The density of a 1-D simulation in the condition that separation $d = 10$ a.u. and temperature $kT = 0.1$ Ha

I increase the temperature, the large thermal fluctuation cover the effect of this correlation, and let us only see correlation in a relative short range. Fig. 5.3 and Fig. 5.4 are graphs with same temperature but different wire separation. Comparing these two figs, I find that the correlation function within one wire is quite similar in the two figures, while the correlation function between two wires separate by 20 a.u. is much weaker than that between two wires separated by 10 a.u.

1-D simulation result

In the exact 1-D case, I cannot plot density like in 2-D case, instead I plot the electron occupation versus wire coordinate graph in one wire to

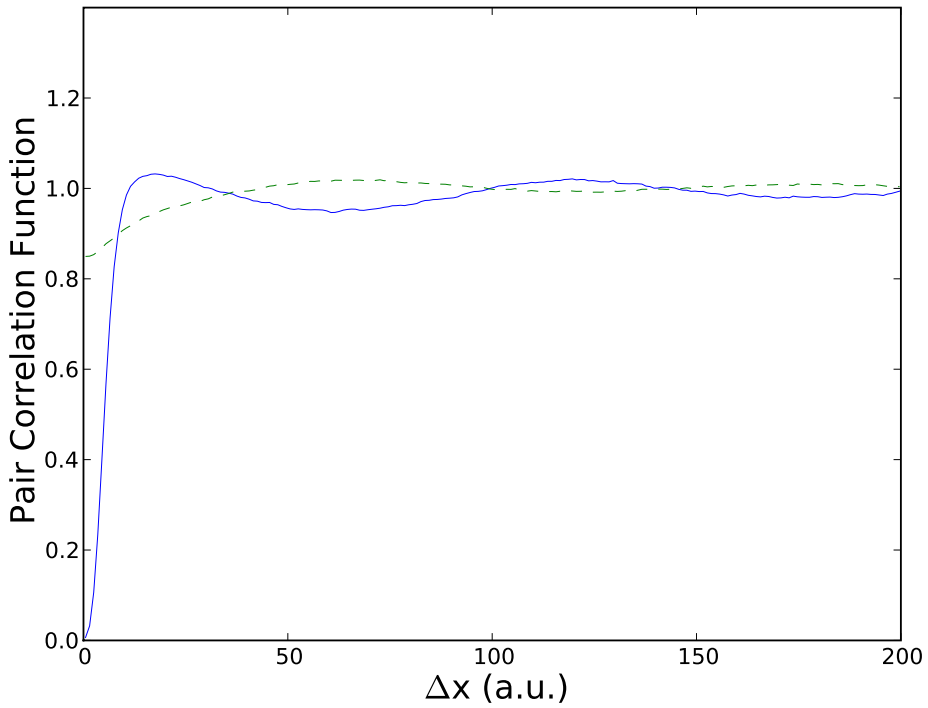

Figure 5.6: This is the density-density pair correlation function in 1D simulation with wire separation $d = 10$ a.u. and temperature $kT = 0.1$ Ha. The blue line represents the pair correlation of two electrons in same wire and the green one refers to the pair correlation function between different wire

see the distribution of electrons. In the simulation I separate the wire into 2200 grids, which are 0.5 a.u. long. Each grid should have 0.025 electrons in average. Fig. 5.5 gives the electron occupation of each grid. I can find that the occupations of electrons in all grids fluctuate around average value 0.025 and the amplitude of the fluctuation is about $\pm 4\%$ of the average value. From this graph, I can also confirm the uniform distribution in 1-D simulation.

Here, I present three corresponding pair correlation function graphs in 1D simulation. Comparing these graph with the 2D case, I can see

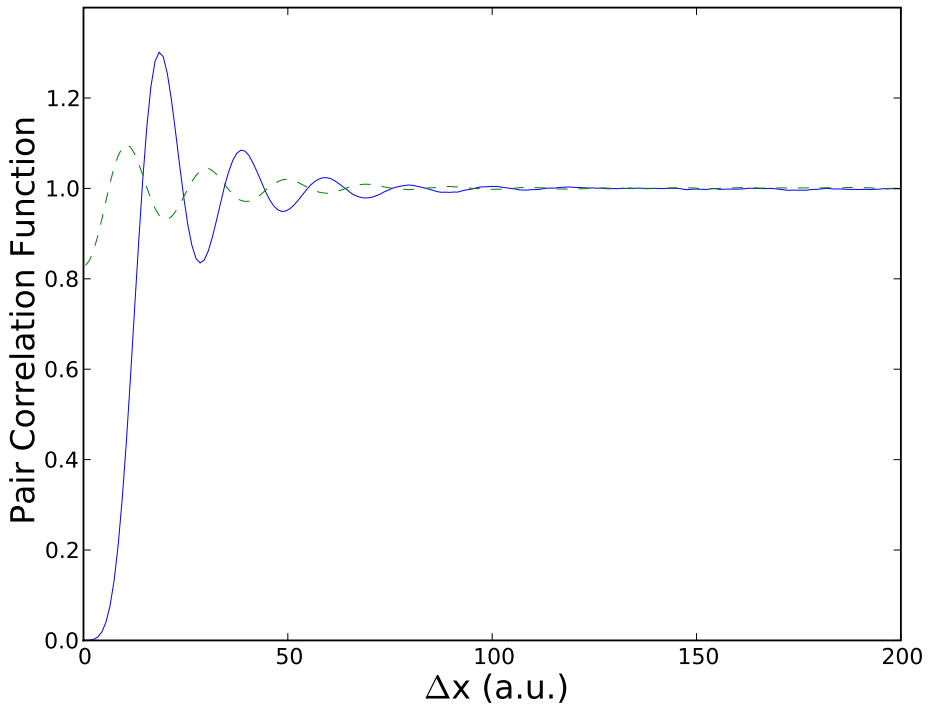

Figure 5.7: This is the density-density pair correlation function in 1D simulation with wire separation $d = 10$ a.u. and temperature $kT = 0.01$ Ha. The blue line represents the pair correlation of two electrons in same wire and the green one refers to the pair correlation function between different wire

that almost all features of the correlation function remain the same. However, in the Fig. 5.6, I find a long correlation signal in the blue lines. Although the amplitude of this signal is not large, it dampened slowly with the increase of Δx. When I go back to 2D simulations, I find that this effect is very weak and I do not treat it as a signal at first, and it becomes much more obvious in 1D simulation. Since it only appears in the simulation with higher temperature($kT = 0.1$ Ha), I guess that this oscillation is related to the thermal fluctuations of the systems.

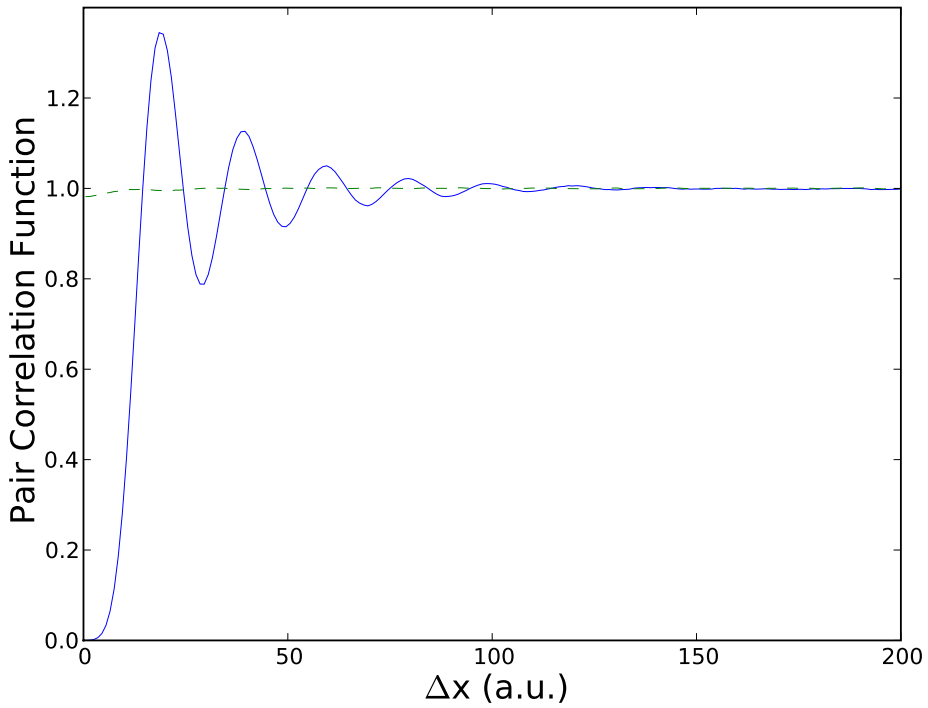

Figure 5.8: This is the density-density pair correlation function in 2D simulation with wire separation $d = 20$ a.u. and temperature $kT = 0.01$ Ha. The blue line represents the pair correlation of two electrons in same wire and the green one refers to the pair correlation function between different wire

Comparison With RPA and QMC Result

After I collect all the density-density correlation function for different wire separation and temperature. I use Eq. (5.5) to calculate the van der Waals interaction. In order to compare with the RPA and QMC results, I make a log-log plot which shows van der Waals interaction per particle as a function of wire separation. Using Eq. (5.3) and atomic unit with my simulation condition , I get,

$$E^{vdW}(d) = -\frac{\sqrt{10}}{16\pi d^2(\ln(2.39d))^{3/2}}, \tag{5.9}$$

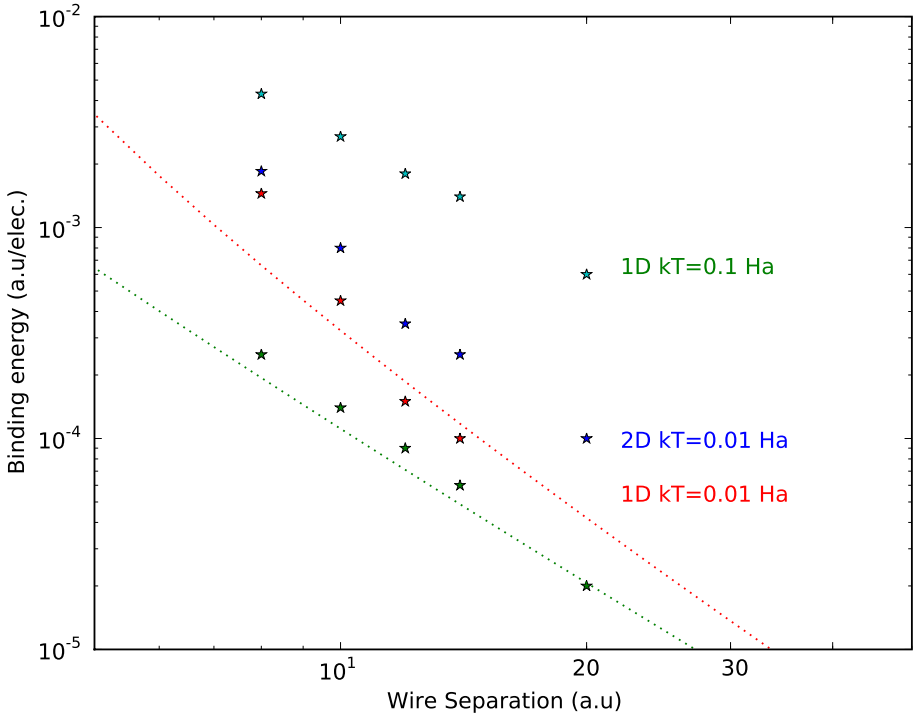

Figure 5.9: Binding energy between two wires plotted as function of wire separation. Green dashed line is the RPA result, and the red dash line is the QMC result. From top to bottom, there are four sets of data, top one is from 1D simulation with $kT = 0.1$ Ha, then the blue one is from 2D simulation with $kT = 0.01$ Ha, the red one is from 1D simulation with $kT = 0.01$ Ha, and finally the bottom data is the theoretical calculation from Eq. (5.2).

which is the green dash line in Fig. 5.9. The the fit ground state QMC result is (Drummond and Needs, 2007),

$$E^{vdW}(d) = -\frac{0.0967}{d^2.17(\ln(0.492d))^{3/2}}. \tag{5.10}$$

From the graph, I can see that both 1D and 2D simulation results at temperature $kT = 0.01$ Ha have similar slope (power law dependance) with QMC result lines which is a little bit steeper than that of RPA results. This implies that both QMC and PIMC results consider the

important correlation effect which is neglected by RPA in this regime. Comparing my 1D and 2D results, the graph shows that 1D simulations always give a lower van der Waals binding energy than 2D simulations and is closer to the QMC curve line, which is also an exact one dimensional simulation. In the 1D simulations $d = 20$ a.u., and $kT = 0.01$ Ha, is not shown on the graph. This is because that the value of van der Waals interaction is so small that it is beyond the accuracy of my simulation. Another important information I want to investigate from this graph is the temperature dependence of van der Waals interaction. From the result data spots of $kT = 0.1$ Ha and $kT = 0.01$ Ha, I can conclude that the interaction increases when I heat up the systems and the slope of higher temperature cases is flatter than that at low temperature.

5.4 Conclusion

In conclusion, I calculated density-density pair correlation functions from PIMC simulations with different temperatures and wire separation. The results show that the correlation effect at low temperature is more clear than that in higher temperature, and the correlation between electrons are very weak when they are far away from each other. I find that the separation power dependence of van der Waals interaction in my results is closer to QMC result, and it totally disagree with the traditional pairwise van der Waals model. Furthermore temperature effects can be exploited from my results: with the increase of temperature, the van der Waals interaction increase.

Chapter 6

SUMMARY

I have looked at quantum many-body systems with different interactions. In these kind of problems, one major difficulty is how to deal with the quantum correlation between interacting particles. The path integral Monte Carlo method is one of the theoretical approximation methods that has been widely used. Comparing the PIMC technique to the other approximation methods, I have showed that PIMC has a lot of advantages: it automatically includes all the correlation effects when applying a proper interaction term in the quantum system and it is a numerically exact method when applied to bosons or classical particles. It also has some restrictions such as it is a finite temperature method, with the decrease of the temperature the sampling efficiency will also decrease, and when applying PIMC to fermions, I need to include fixed node approximations which depend on the selection of trial density matrix. In this dissertation, I introduced the basic physics ideas behind the PIMC method and applied it to three quantum systems. In this chapter I review the content of previous chapters.

In Chapter 2, I reviewed in detail the path-integral Monte Carlo method, how it relates to the quantum many-body systems, and how to use it to calculate the properties of quantum many body systems. I first discussed the mathematical basis thermal density matrix of path integrals and the relationship between path integrals and physical properties. Then I showed the details about how to express the thermal expec-

tation value of a quantum mechanics operator in terms of path integral expressions. This integral form applies to bosonic systems by including permutations of identical particles. Extension of bosonic PIMC to fermion systems can be made by the fixed node approximation, which prevents paths from crossing the nodes of a trial density matrix. I also discussed how to use Metropolis sampling method to perform single slices sampling, multi-slice sampling and permutation sampling. Finally, I also indicate how to calculate physical properties with the path-integral Monte Carlo method. In Chapter 3-5, I have showed how PIMC simulations have helped us understand the quantum many-body problems by mapping the original problem of quantum statistical-mechanics into a domain that is easier to understand.

In Chapter 3, I have demonstrated a PIMC algorithm for computing exchange-splitting energy in double quantum dots. I found that the exchange-splitting energy arises from instantons in the bosonic path integral. Thus I can calculate the splitting energy by dealing with the permutation in the bosonic simulation. My splitting energy has a good agreement with the results calculated by the direct diagonalization method. To learn more, I collected the two-particle density and defined the double occupation of this system from which I calculate the hopping matrix element t_r and renormalized on-site energy $U_r - V_r$. I have shown that both t_r and $U_r - V_r$ have a dramatic decrease at large separation comparing with the normal Hubbard model value. I also collected data on these paths when they are crossing each other, which include double occupation and the correlation hole. I found that simultaneous crossing occurs more often when two quantum dots are close to each other, while further

separated dots are more likely to have instantons with double occupations. Finally, I have demonstrated the versatility of the algorithm with the inclusion of magnetic fields.

In Chapter 4, I used PIMC to simulate a 2-D parabolic dot. Comparing my binding energy results with another theoretical method, director diagonalization, I showed that the PIMC method include all the correlation effect thus get more accurate results. Then I applied PIMC to calculate the energy, dipole moment, polarizability and hyperpolarizability of excitonic systems in different quantum dot samples. From the result I successfully give the PL spectra for different dots in both growth and transverse direction (Fig. 4.4 and 4.6). Comparing my numbers (growth/axial direction of the graded dot) to the existing experimental results, I find the polarizability and the energy shifts in my simulation match very well. Furthermore I investigated the same quantities for quantum dots of different shape and composition to study how these factors affect the PL spectra. From this I infer that it is possible to change the intrinsic dipole moment direction by changing the dot geometry as suggested by recent experiments. Another important part of this research is the study of the influence of hyperpolarizability on the PL spectra. The hyperpolarizability is the higher order term which was always ignored in previous research. I showed my method can handle it and observed that in the axial direction due to the smaller dimension of the dot ($\sim$ 5 nm) hyperpolarizabilities are not large enough. But in transverse direction, with is much larger dimensions $\sim$ 23 nm, the hyperpolarizability does change the spectra with large electric fields. I added a piezoelectric field to the dots and found how vertical electric

field affect the anisotropic effect of lateral polarizability.

In Chapter 5, I used PIMC method to calculate the van der Waals interaction between two wires with different wire separation and temperature. First I showed the how to calculate the van der Waals interaction from the pair correlation function. Then I simulated the system with PIMC using 1D and 2D Hamiltonians that help us understand interactions between thin metallic wires. The average density of electrons in wires are collected in all simulations, which gives us a qualitative criteria for sampling efficiency in one aspect. I also plotted the density-density pair correlation function in each case. From the graphs I concluded that correlation effect in low temperature is more clear than that in higher temperature, and the correlation between electrons are very weak when they are far away from each other. When I compare PIMC result with RPA and ground-state QMC results, I find that the interaction-separation power law of my result is closer to QMC result, and it totally disagrees with a naive pairwise van der Waals model. I also show that the van der Waal interaction from 1D simulation are lower than that from 2D simulation, thus closer to the QMC results. Furthermore, temperature effect can be seen from my results: with the increase of temperature, the van der Waals interaction increase. The temperature effect can in one aspect be used to explain that fact that PIMC result has a higher energy value than the QMC results. More work can be done to theoretically calculate the temperature effect in RPA and compare directly to my simulation results.

Appendix A

Path Integral Monte Carlo Method For Quantum Dots

I use PIMC to solve for correlated electrons and holes (Harowitz *et al.*, 2005). The thermal density matrix can be calculated from the imaginary time path integral (Ceperley, 1995; Shumway and Ceperley, 2000),

$$\begin{aligned}\rho(R,R';\beta) &= \frac{1}{\boldsymbol{Z}}\langle R|e^{-\beta\hat{H}}|R'\rangle \\ &= \frac{1}{\boldsymbol{Z}}\int \mathcal{D}R(\tau)\,\exp\left(-\frac{1}{\hbar}S_E[R(\tau)]\right), \\ R(0) &= R' \\ R(\beta\hbar) &= R\end{aligned} \tag{A.1}$$

where $R = (\boldsymbol{r}_1, \boldsymbol{r}_2, \ldots, \boldsymbol{r}_{3N})$ represents the 3N position coordinates of all the quantum particles, and $\boldsymbol{Z}$ is the partition function that normalizes the density matrix, $\mathrm{Tr}\,\rho = 1$. The integral in the second line of the equation is the sum over random walks $R(\tau)$ taking place in imaginary time τ, starting at R' at imaginary time $\tau = 0$ and ending at R at imaginary time $\tau = \beta\hbar$. The paths are weighted by the Euclidean action $S_E[R(\tau)]$, which is the functional of the path $R(\tau)$,

$$S_E[R(\tau)] = \int_0^{\beta\hbar}\left(\sum_{i=1}^{N}\frac{1}{2}\boldsymbol{m}_i^*\dot{\boldsymbol{r}}_i{}^2 + V[R(\tau)]\right)d\tau \tag{A.2}$$

The quantity in the integrand is the Euclidean Lagrangian, $\boldsymbol{L} = T + V$. The potential energy $V[R(\tau)]$ includes all the external potentials and interactions between particles. The diagonal terms of the density matrix is taken by setting $R = R'$,which just closes the loop of the path, and I can get the trace by summing over all paths.Therefore the statistical quantum mechanics expectation values can be calculated as a weighted sum

over closed paths. If the particles are identical, there is an additional sum over permutations

$$\rho(R,R';\beta)=\frac{1}{\boldsymbol{Z}}\frac{1}{N!}\sum_{P}(-1)^{P}\int \mathcal{D}R(\tau)e^{-\frac{1}{\hbar}S_{E}[R(\tau)]} \tag{A.3}$$
$$R(0)=R'$$
$$R(\beta\hbar)=PR$$

which symmetrizes or antisymmetrizes the many-body wavefunction. The factor $(-1)^{P}$ gives minus signs for permutations of antisymmetric fermions.

There are two major advantages for using the imaginary-time path integral, Eq. (A.1), to simulate the quantum dot systems. First this method is a many-body formalism. In the path integral approach, no single particle approximation is made, so correlation effects are included automatically. Second the path integral method naturally averages over all quantum and thermal fluctuations. In Eq. (A.1), the thermal average over many-body energy eigenstates is implicit in the path integral. So I can directly calculate the observables in canonical ensemble rather than finding the many-body energies and wavefunctions for each eigenstate individually

Appendix B

Perturbative Response Theory

I use standard perturbation theory techniques in imaginary time to study the response of the system to electric fields. It is important to note that, unlike diagrammatic theories (Li and Xia, 2000; Ritter *et al.*, 2007), interactions are treated essentially exactly in path integral monte carlo or PIMC (due to the large Trotter number and very accurate short-time propagator), and I only use perturbation to describe an external potential that is, by definition (Eq. 4.1), weak. Most textbooks do not emphasize non-linear response and its connections to PIMC. For completeness, I give a brief derivation of the key equations and explain their use in PIMC in this section.

Consider the effect of a perturbation in imaginary time on the path integral. Let the perturbation take the form,

$$\Delta S = -\int_0^{\beta\hbar} e^{i\tau\omega_n} \boldsymbol{\mathcal{E}} \cdot \mathbf{d}(\tau)\, d\tau, \tag{B.1}$$

where $i\omega_n = 2\pi i n k_B T$ and the total dipole moment $\boldsymbol{d}(\tau)$ is a function of the N-particle imaginary-time path,

$$\boldsymbol{d}(\tau) = \sum_{i=1}^{N} q_i \boldsymbol{r}_i(\tau). \tag{B.2}$$

In practice, it is convenient to work with the Fourier transform,

$$\boldsymbol{d}(i\omega_n) = \int_0^{\beta\hbar} e^{i\tau\omega_n} \mathbf{d}(\tau)\, d\tau, \tag{B.3}$$

Note that $\boldsymbol{d}(i\omega_n)$ is a functional of a particular path $\mathbf{R}(\tau)$; taking averages over all unperturbed paths yields,

$$\begin{aligned}\langle \boldsymbol{d}(i\omega_n)\rangle_0 &= \int \mathcal{D}\mathbf{R}(\tau)\left(\int_0^{\beta\hbar} e^{i\omega_n\tau}\mathbf{d}(\tau)\,d\tau\right) e^{-\frac{1}{\hbar}S_0[\mathbf{R}(\tau)]} \\ &= \begin{cases}\mathbf{d}_0 & \text{if} \quad i\omega_n = 0, \\ 0 & \text{otherwise}.\end{cases}\end{aligned} \tag{B.4}$$

To see that this average vanishes for non-zero frequency, I note that $\langle \mathbf{d}(i\omega_n)\rangle_0 \rightarrow e^{i\omega_n\tau'}\langle \mathbf{d}(i\omega_n)\rangle_0$ when the origin of imaginary time is shifted $\tau \rightarrow \tau + \tau'$. Since this is a symmetry of the path integral, the expectation value must vanish for $i\omega_n \neq 0$. Note that a subscript "0" is used to indicate an average over unperturbed paths. In terms of $\boldsymbol{d}(i\omega_n)$, the perturbation, Eq. (B.1), takes the simple form

$$\Delta S = -\boldsymbol{\mathcal{E}}\cdot\mathbf{d}(i\omega_n) \tag{B.5}$$

In the presence of the perturbing field, the value of the dipole moment averaged over all paths is given by

$$\begin{aligned}\langle \boldsymbol{d}(i\omega_{n'})\rangle &= \frac{\int \mathcal{D}\boldsymbol{R}(\tau)\,\boldsymbol{d}(i\omega_{n'})\,e^{-\frac{1}{\hbar}(S_0[\mathbf{R}(\tau)]+\Delta S)}}{\int \mathcal{D}\boldsymbol{R}(\tau)\,e^{-\frac{S_0[\mathbf{R}(\tau)]}{\hbar}}e^{-\frac{\Delta S}{\hbar}}} \\ &= \frac{\left\langle \boldsymbol{d}(i\omega_{n'})e^{-\frac{\Delta S}{\hbar}}\right\rangle_0}{\left\langle e^{-\frac{\Delta S}{\hbar}}\right\rangle_0}\end{aligned} \tag{B.6}$$

Following standard perturbation techniques, I expand the perturbing exponentials in powers of $\boldsymbol{\mathcal{E}}$. For $i\omega_n \neq 0$, many of these terms are zero, by the argument following Eq. (B.4). The surviving, non-zero terms are,

$$\begin{aligned}\langle d_\alpha(i\omega_{n'})\rangle &= \frac{1}{\hbar}\langle d_\alpha(i\omega_{n'})d_\beta(i\omega_n)\rangle_0\,\mathcal{E}_\beta \\ &+ \frac{1}{2!\hbar^2}\langle d_\alpha(i\omega_{n'})d_\beta(i\omega_n)d_\gamma(i\omega_n)\rangle_0\,\mathcal{E}_\beta\mathcal{E}_\gamma \\ &+ \frac{1}{3!\hbar^3}\langle d_\alpha(i\omega_{n'})d_\beta(i\omega_n)d_\gamma(i\omega_n)d_\delta(i\omega_n)\rangle_0\,\mathcal{E}_\beta\mathcal{E}_\delta\mathcal{E}_\gamma \\ &+ \ldots .\end{aligned} \tag{B.7}$$

Even these average are non-zero are only non-zero if the frequencies add to zero, that is, $i\omega_{n'} = -i\omega_n$ for the linear term, $i\omega_{n'} = -2i\omega_n$ for the quadratic term, etc.

Comparing Eqs. (4.2) and (B.7) and taking the zero-frequency limit, I see that the static polarizability and hyperpolarizabilities are given by

$$\Gamma^2_{\alpha\beta} = \lim_{i\omega_n\to 0}\frac{1}{\hbar}\langle d_\alpha(-i\omega_n)d_\beta(i\omega_n)\rangle_0, \tag{B.8a}$$

$$\Gamma^3_{\alpha\beta\gamma} = \lim_{i\omega_n\to 0}\frac{1}{\hbar^2}\langle d_\alpha(-2i\omega_n)d_\beta(i\omega_n)d_\gamma(i\omega_n)\rangle_0, \tag{B.8b}$$

$$\Gamma^4_{\alpha\beta\gamma\delta} = \lim_{i\omega_n\to 0}\frac{1}{\hbar^3}\langle d_\alpha(-3i\omega_n)d_\beta(i\omega_n)d_\gamma(i\omega_n)d_\delta(i\omega_n)\rangle_0. \tag{B.8c}$$

Since the correlation functions are only defined at discrete Matsubara frequencies, the limit must be understood as fitting an analytic function to the discrete data and extrapolating to zero-frequency. Such a procedure assumes that all non-analytic features, such as poles on the real frequency axis, are sufficiently far from zero that the extrapolation is feasible. In practice, this means the temperature must be somewhat less than the smallest energy spacings that contribute significantly to the desired correlation function. For example, to compute the polariz-

ability of a quantum dot, I must perform the PIMC simulations with $k_B T$ somewhat less than the electron and hole energy spacing of the dots.

It is very straightforward to collect the averages in Eqs. (B.8a–B.8c) in a PIMC simulation by collecting $\mathbf{d}(\tau)$ for a path configuration, performing a fast-Fourier transform, Eqs. (B.2–B.3), multiplying terms for several small, non-zero frequencies, Eqs. (B.8a–B.8c), and averaging these values for many path configurations. In this work, I collected averages for fifty frequencies ($i\omega_1$ to $i\omega_5 0$). Because the discretization of the path cuts off the high frequency data, one should be careful not to use frequencies too close to the time resolution of the discretized path. In particular, the frequency $-3i\omega_n$ in Eq. (B.8c) should not be used for $n > N_{\text{trotter}}/6$.

If periodic boundary conditions are present, it is better to use the imaginary-time polarization current,

$$\mathbf{J}(\tau) = \frac{d}{d\tau}\mathbf{d}(\tau). \tag{B.9}$$

With an integration-by-parts and Eq. (B.3), I have $\mathbf{J}(i\omega_n) = -i\omega_n \mathbf{d}(i\omega_n)$, so Eqs. (B.8a–B.8c) become,

$$\Gamma^2_{\alpha\beta} = \lim_{i\omega_n \to 0} \tfrac{1}{\hbar\omega_n^2} \big\langle J_\alpha(-i\omega_n) J_\beta(i\omega_n) \big\rangle_0, \tag{B.10a}$$

$$\Gamma^3_{\alpha\beta\gamma} = \lim_{i\omega_n \to 0} \tfrac{i}{2\hbar^2\omega_n^3} \big\langle J_\alpha(-2i\omega_n) J_\beta(i\omega_n) J_\gamma(i\omega_n) \big\rangle_0, \tag{B.10b}$$

$$\Gamma^4_{\alpha\beta\gamma\delta} = \lim_{i\omega_n \to 0} \tfrac{-1}{3\hbar^3\omega_n^4} \big\langle J_\alpha(-3i\omega_n) J_\beta(i\omega_n) J_\gamma(i\omega_n) J_\delta(i\omega_n) \big\rangle_0. \tag{B.10c}$$

In the present work, I use this more general formalism, even though my dots are isolated.

Appendix C

Raw Simulation Data for Stark Effect Study

Quantities of interest for three pyramid-shaped dots are tabulated in Tables I and II and for a lens-shaped dot in Tables III and IV. Energy, intrinsic dipole moments, polarizabilities and hyperpolarizabilities in growth direction are given in Tables I and III. Transverse polarizabilities and hyperpolarizabilities are given in Tables II and IV.

Table C.1: Energy, dipole moment, polarizability, and hyperpolarizability correlations of the excitonic systems for three pyramid shaped dots (order: uniform, peaked, graded) for axial field

excitonic system	$(E \pm \delta E)$ (meV)	$(P_z \pm \delta P_z)$ (meV/(kV/cm))	$(\alpha_z \pm \delta\alpha_z)$ (meV/(kV/cm)^2)	$(\beta_z \pm \delta\beta_z)$ (meV/(kV/cm)^3)	$(\gamma_z \pm \delta\gamma_z)$ (meV/(kV/cm)^4)
X^0	1.40339(5) $\times 10^3$	8.04(4) $\times 10^{-3}$	1.012(1) $\times 10^{-3}$	-5(2) $\times 10^{-8}$	5(2) $\times 10^{-8}$
X^+	1.40307(6) $\times 10^3$	1.10(4) $\times 10^{-3}$	9.26(1) $\times 10^{-4}$	9(6) $\times 10^{-8}$	1.3(6) $\times 10^{-8}$
X^-	1.39971(6) $\times 10^3$	1.022(4)$\times 10^{-2}$	8.95(1) $\times 10^{-4}$	-8(5) $\times 10^{-8}$	4(1)$\times 10^{-8}$
XX	1.40063(7) $\times 10^3$	4.63(4) $\times 10^{-3}$	8.44(1) $\times 10^{-4}$	-9(4) $\times 10^{-8}$	4(2)$\times 10^{-8}$
X^0	1.20774(6) $\times 10^3$	2.71(2) $\times 10^{-3}$	2.783(1) $\times 10^{-4}$	-2.8(2) $\times 10^{-8}$	2.1(9)$\times 10^{-9}$
X^+	1.20668(7) $\times 10^3$	1.27(2) $\times 10^{-3}$	2.682(2) $\times 10^{-4}$	-2.2(3) $\times 10^{-8}$	1.7(8)$\times 10^{-9}$
X^-	1.20344(7) $\times 10^3$	3.12(2) $\times 10^{-3}$	2.673(2) $\times 10^{-4}$	-3.9(6) $\times 10^{-8}$	2.3(9)$\times 10^{-9}$
XX	1.20441(7) $\times 10^3$	1.96(2) $\times 10^{-3}$	2.681(1) $\times 10^{-4}$	-2.8(6) $\times 10^{-8}$	1.1(4)$\times 10^{-9}$
X^0	1.26407(6) $\times 10^3$	6.35(3) $\times 10^{-3}$	3.912(2) $\times 10^{-4}$	6(2) $\times 10^{-8}$	7(2)$\times 10^{-9}$
X^+	1.26416(7) $\times 10^3$	1.69(2) $\times 10^{-3}$	3.603(2) $\times 10^{-4}$	1.0(1)$\times 10^{-7}$	5(2)$\times 10^{-9}$
X^-	1.25987(6) $\times 10^3$	8.41(3) $\times 10^{-3}$	3.602(2) $\times 10^{-4}$	1.0(6)$\times 10^{-8}$	1.1(4)$\times 10^{-8}$
XX	1.26140(7) $\times 10^3$	4.13(2) $\times 10^{-3}$	3.401(2) $\times 10^{-4}$	2.6(8)$\times 10^{-8}$	4(2)$\times 10^{-9}$

Table C.2: Transverse polarizability and hyperpolarizability correlations of the excitonic systems for pyramid shaped dots (order: uniform, peaked, graded).

excitonic system	$(\alpha_x \pm \delta\alpha_x)$ (meV/(kV/cm)^2)	$(\beta_x \pm \delta\beta_x)$ (meV/(kV/cm)^3)	$(\gamma_x \pm \delta\gamma_x)$ (meV/(kV/cm)^4)
X^0	9.47(1)$\times 10^{-3}$	7(2)$\times 10^{-6}$	5(2)$\times 10^{-6}$
X^+	4.73(2)$\times 10^{-3}$	2.28(2)$\times 10^{-5}$	1.0(4)$\times 10^{-5}$
X^-	5.35(1)$\times 10^{-3}$	1(2)$\times 10^{-6}$	1.2(8)$\times 10^{-5}$
XX	4.94(2)$\times 10^{-3}$	2(2)$\times 10^{-6}$	1.6(3)$\times 10^{-6}$
X^0	6.79(1)$\times 10^{-3}$	3(5)$\times 10^{-6}$	1.6(9)$\times 10^{-6}$
X^+	3.50(1)$\times 10^{-3}$	2(2)$\times 10^{-6}$	2(1)$\times 10^{-6}$
X^-	3.60(1)$\times 10^{-3}$	3(4)$\times 10^{-6}$	5.4(8)$\times 10^{-6}$
XX	2.98(1)$\times 10^{-3}$	-3(4)$\times 10^{-6}$	-8(4)$\times 10^{-7}$
X^0	5.15(1)$\times 10^{-3}$	1.2(4)$\times 10^{-6}$	7(4)$\times 10^{-7}$
X^+	3.09(1)$\times 10^{-3}$	2.6(1)$\times 10^{-6}$	1.3(1)$\times 10^{-6}$
X^-	2.98(1)$\times 10^{-3}$	-2(7)$\times 10^{-7}$	1.2(9)$\times 10^{-6}$
XX	2.57(1)$\times 10^{-3}$	7(6)0$\times 10^{-7}$	-8(1)$\times 10^{-7}$

Table C.3: Energy, dipole moment, polarizability, and hyperpolarizability correlations of the excitonic systems for lens shaped dot for axial field

excitonic system	$(E \pm \delta E)$ (meV)	$(P_z \pm \delta P_z)$ (meV/(kV/cm))	$(\alpha_z \pm \delta\alpha_z)$ (meV/(kV/cm)^2)	$(\beta_z \pm \delta\beta_z)$ (meV/(kV/cm)^3)	$(\gamma_z \pm \delta\gamma_z)$ (meV/(kV/cm)^4)
X^0	1.13593(6)$\times 10^3$	-7.30(3)$\times 10^{-3}$	5.042(2)$\times 10^{-4}$	-1.40(9)$\times 10^{-7}$	-9(3)$\times 10^{-11}$
X^+	1.13382(6)$\times 10^3$	-1.253(3)$\times 10^{-2}$	4.532(4)$\times 10^{-4}$	-2(1)$\times 10^{-8}$	4.2(8) $\times 10^{-10}$
X^-	1.13287(6)$\times 10^3$	-2.70(3)$\times 10^{-3}$	4.634(3)$\times 10^{-4}$	-1.4(3)$\times 10^{-7}$	-8(3)$\times 10^{-10}$
XX	1.13258(6)$\times 10^3$	-7.51(3)$\times 10^{-3}$	4.322(7)$\times 10^{-4}$	-6(3)$\times 10^{-8}$	-1.5(2) $\times 10^{-9}$

Table C.4: Transverse polarizability and hyperpolarizability correlations of the excitonic systems for lens shaped dot.

excitonic system	$(\alpha_x \pm \delta\alpha_x)$ (meV/(kV/cm)^2)	$(\beta_x \pm \delta\beta_x)$ (meV/(kV/cm)^3)	$(\gamma_x \pm \delta\gamma_x)$ (meV/(kV/cm)^4)
X^0	8.85(2)$\times 10^{-3}$	1.1(3)$\times 10^{-5}$	4(2)$\times 10^{-6}$
X^+	4.12(2)$\times 10^{-3}$	-1.4(3)$\times 10^{-5}$	1.1(5)$\times 10^{-5}$
X^-	4.94(1)$\times 10^{-3}$	5(2)$\times 10^{-6}$	2.5(7)$\times 10^{-6}$
XX	3.50(1)$\times 10^{-3}$	9(3)$\times 10^{-6}$	1.6(2)$\times 10^{-6}$

Appendix D

Two-Site Hubbard Model And Formation of Renormalized Hopping Constant and Interaction

In this part, I want to show how to calculate hopping matrix element t and renormalized on-site repulsion $U - V$ from a two-site Hubbard model. The Hamiltonian is now made up of three components. The first component is the hopping integral. The hopping integral is typically represented by the letter t, because it represents the kinetic energy of electrons hopping between two sites. The second term in the Hubbard model is then the on-site repulsion, typically represented by the letter U. It represents the potential energy when two electrons stay in the same site. The third term is the inter-site repulsion; I use V to represent the Coulomb interaction when two electrons are in different sites. Written out in second quantization notation, the Hubbard Hamiltonian then takes the form:

$$H = -t \sum_{\sigma} (a^{\dagger}_{1,\sigma} a_{2,\sigma} + a^{\dagger}_{2,\sigma} a_{1,\sigma}) + U \sum_{i=1}^{2} n_{i\uparrow} n_{i\downarrow} + V \sum_{\sigma,\sigma'} n_{1,\sigma} n_{2,\sigma'}, \tag{D.1}$$

where number $1, 2$ is the site which electron is in, and σ represent the spin of the electrons. I expand the hamiltonian in four basis, $(\uparrow\downarrow, 0)$, $(0, \uparrow\downarrow)$, $(\uparrow, \downarrow)$ and $(\downarrow, \uparrow)$ and get the matrix expression:

$$H = \begin{pmatrix} U & 0 & -t & -t \\ 0 & U & -t & -t \\ -t & -t & V & 0 \\ -t & -t & 0 & V \end{pmatrix}. \tag{D.2}$$

I can easily solve this matrix, and the lowest two eigenvalues are $E_0 = V - \frac{4t^2}{U-V}$, and $E_1 = V$. I can also get the corresponding eigenstates: $\psi_0 = \frac{1}{\sqrt{2(1+\frac{(U-V)^2}{4t^2})}}((\uparrow\downarrow,0)+(0,\uparrow\downarrow)+\frac{U-V}{2t}((\uparrow,\downarrow)+(\downarrow,\uparrow)))$ and $\psi_1 = \frac{1}{\sqrt{2}}((\uparrow,\downarrow) - (\downarrow,\uparrow))$. As I predicted, the ground state is a space symmetric state and excited state is space antisymmetric. From the equation above, I can get the splitting energy $J = \frac{4t^2}{U-V}$ and double occupation probability of ground state: $x_D = \frac{1}{1+\frac{(U-V)^2}{4t^2}}$. From PIMC method, I can calculate J and x_D. Inverting the equation above, I get $U - V = J(\frac{1}{x_D} - 1)$ and $t = \frac{J}{2}\sqrt{(\frac{1}{x_D} - 1)}$.

Appendix E

Form of the Discretized Path Integral and the Action

The partition function for the effective mass Hamiltonian, Eq. (3.1), can be written as an imaginary time path integral (Feynman, 1972; Ceperley, 1995; Harowitz *et al.*, 2005),

$$Z = \int \mathcal{D}R(\tau) e^{-\frac{1}{\hbar} S_E[R(\tau)]}. \tag{E.1}$$

The path integral $\int \mathcal{D}R(\tau)$ and Euclidean action S_E are easiest to define in the discretized form I used in the Monte Carlo integration. By dividing imaginary time into N_T discrete steps, each of length $\Delta\tau = \beta\hbar/N_T$, the path $R(\tau)$ becomes an array of positions ("beads") $\mathbf{r}_{ij}$, where i indicates the slice number ($0 \le i < N_T$) and $j = 1, 2$ labels the two electrons. Then the path integral becomes a multiple integral over all bead positions,

$$\int \mathcal{D}R(\tau) \rightarrow \prod_{i=0}^{N_T-1} \int d\mathbf{r}_{1j} \int d\mathbf{r}_{2j}. \tag{E.2}$$

The action S_E represents the terms in the effective mass Hamiltonian and is a function of the bead coordinates,

$$\begin{aligned} S_E \;=\; & \sum_{i=0}^{N_T-1} \Bigg[\frac{m^* |\mathbf{r}_{i+1\,1} - \mathbf{r}_{i\,1}|^2}{2\,\Delta\tau} + \frac{m^* |\mathbf{r}_{i+1\,2} - \mathbf{r}_{i\,2}|^2}{2\,\Delta\tau} \\ & + 2\ln(2\pi\,\Delta\tau/m^*) + V_{\rm ext}(\mathbf{r}_{i\,1})\Delta\tau + V_{\rm ext}(\mathbf{r}_{i\,2})\Delta\tau \\ & + u_{\rm coul}(\mathbf{r}_{i+1\,1}, \mathbf{r}_{i+1\,1}, \mathbf{r}_{i\,2}, \mathbf{r}_{i\,2}; \Delta\tau) \Bigg]. \end{aligned} \tag{E.3}$$

The first three terms (which explicitly contain m^*) are the kinetic action and are derived from the free particle propagator in two dimensions.

The next two terms are the action for the confining potential, $V_{\rm ext}(\mathbf{r})$, evaluated in the primitive approximation (Ceperley, 1995). The last term is the pair Coulomb action (Ceperley, 1995), which I have fit to a short-time approximation of the Coulomb propagator for the imaginary time interval $\Delta\tau$. Because of special symmetry of the Coulomb potential, this propagator is only a function of two coordinates, $q_i = (|\mathbf{r}_{i+1\,1} - \mathbf{r}_{i+1\,2}| + |\mathbf{r}_{i\,1} - \mathbf{r}_{i\,2}|)/2$ and $s_i^2 = |(\mathbf{r}_{i+1\,1} - \mathbf{r}_{i+1\,2}) - (\mathbf{r}_{i\,1} - \mathbf{r}_{i\,2})|^2$. For simplicity, I have dropped the s^2 dependence; this approximation is exact as $\Delta\tau \to 0$. I evaluated the short time Coulomb propagator using the high-accuracy Trotter method of Schmidt and Lee (1995) and stored tabulated values of $u_{\rm coul}(q;\Delta\tau)$ on a grid for efficient evaluation during my Monte Carlo simulations.

To perform the trace implicit in Eq. (E.1), I identify slice N_T with slice 0 in Eq. (E.3) by setting $\mathbf{r}_{N_T\,1} = \mathbf{r}_{0\,1}$ and $\mathbf{r}_{N_T\,2} = \mathbf{r}_{0\,2}$. The division of the partition function into spatially symmetric Z_+ and antisymmetric Z_- parts may be accomplished by summing over permutations $P = \mathcal{I}, \mathcal{P}$, as in Eq. (A.1). Permuting configurations ($P = \mathcal{P}$) are handled by setting $\mathbf{r}_{N_T\,1} = \mathbf{r}_{0\,2}$ and $\mathbf{r}_{N_T\,2} = \mathbf{r}_{0\,1}$ in Eq. (E.3).

BIBLIOGRAPHY

Anderson, J. B., "A random walk simulation of the Schrödinger equation: H_3^+", J. Chem. Phys. **63**, 1499 (1975).

Anderson, J. B., "Fixed-node quantum Monte Carlo", Int. Rev. Phys. Chem. **14**, 85 (1995).

Ashoori, R. C., H. L. Stormer, J. S. Weiner, L. N. Pfeiffer, S. J. Pearton, K. W. Baldwin, and K. W. West, "Single-electron capacitance spectroscopy of discrete quantum levels", Phys. Rev. Lett. **68**, 3088 (1992).

Ashoori, R. C., H. L. Stormer, J. S. Weiner, L. N. Pfeiffer, S. J. Pearton, K. W. Baldwin, and K. W. West, "N-electron ground state energies of a quantum dot in magnetic field", Phys. Rev. Lett. **71**, 613 (1993).

Banerjee, S. and K. A. Shore, "Biexciton blue stark shift in semiconductor quantum dots", J. Appl. Phys. **97**, 123101 (2005).

Barenco, A., C. H. Bennett, R. Cleve and D. P. DiVincenzo, "Elementary gates for quantum computation", Phys. Rev. A **52**, 3457 (1995).

Barker, J. A. and E. P. O'Reilly, "Theoretical analysis of electron-hole alignment in InAs-GaAs quantum dots", Phys. Rev. B **61**, 13 840 (2000).

Baughman, R. H., A. A. Zakhidov and W. A. de Heer, "Carbon nanotubes - the route toward applications", Science **297**, 787 (2002).

Baym, G. and N. D. Mermin, "Determination of thermodynamic Green's functions", J. Math. Phys. **2**, 232 (1961).

Bennett, A. J. and R. B. Patel, "Giant stark effect in the emission of single semiconductor quantum dots", Appl. Phys. Lett. **97**, 031104 (2010).

Bennett, C. H., "Quantum information and computation", Phys. today **48**, 24 (1995).

Bernu, B., L. Cândido and D. M. Ceperley, "Exchange frequencies in the 2d wigner crystal", Phys. Rev. Lett. **86**, 870 (2001).

Berry, M. V., "Quantal phase factors accompanying adiabatic changes", Proc. R. Soc. A **392**, 1802, 45 (1984).

Burkard, G., D. Loss and D. P. DiVincenzo, "Coupled quantum dots as quantum gates", Phys. Rev. B **59**, 2070 (1999).

Ceperley, D. M., "Fermion nodes", jsp **63**, 1237–1267 (1991).

Ceperley, D. M., "Path-integral calculations of normal liquid ^{3}He", Phys. Rev. Lett. **69**, 331 (1992).

Ceperley, D. M., "Path integrals in the theory of condensed helium", Rev. Mod. Phys. **67**, 279 (1995).

Ceperley, D. M. and B. J. Alder, "Quantum Monte Carlo", Science **231**, 555 (1986).

Ceperley, D. M. and G. Jacucci, "Calculation of exchange frequencies in bcc He^3 with the path-integral Monte Carlo method", Phys. Rev. Lett. **58**, 16, 1648 (1987).

Cornet, C., J. Even and S. Lousliche, "Exciton and biexciton binding and vertical stark effect in a model lens-shaped quantum box: Application to InAs/InP quantum dots", definition **344**, 457 (2005).

Dion, M., H. Rydberg and E. schröder, "Van der Waals density functional for general geometries", Phys. Rev. Lett. **92**, 246401 (2004).

Divincenzo, D. P., "Quantum computation", Science **270**, 255 (1995).

Dobson, J. F. and J. Wang, "Successful test of a seamless van der Waals density functional", Phys. Rev. Lett. **82**, 2123 (1999).

Dobson, J. F., A. White and A. Rubio, "Asymptotics of the dispersion interaction: Analytic benchmarks for van der waals energy functionals", Phys. Rev. Lett. **96**, 073201 (2006).

Drummond, N. D. and R. J. Needs, "van der waals interactions between thin metallic wires and layers", Phys. Rev. Lett. **99**, 166401 (2007).

Feynman, R. P., "Atomic theory of the λ transition in Helium", Phys. Rev **91**, 1291 (1953).

Feynman, R. P., *Statistical Mechanics* (Addison-Wesley, Reading, MA, 1972).

Finley, J. J., A. D. Ashmore, A. Lemaitre, D. J. Mowbray and M. S. Skolnick, "Charged and neutral exciton complexes in individual self-assembled In(Ga)As quantum dots", Phys. Rev. B **63**, 073307 (2001).

Finley, J. J., M. Sabathil, P. Vogl and G. Abstreiter, "Quantum-confined stark shifts of charged exciton complexes in quantum dots", Phys. Rev. B **70**, 201308(R) (2004).

Foulkes, W. M. C., L. Mitas, R. J. Needs and G. Rajagopal, "Quantum Monte Carlo simulations of solids", Rev. Mod. Phys. **73**, 33 (2001).

Fry, P. W., I. E. Itskevich and D. J. Mowbray, "Inverted electron-hole alignment in InAs-GaAs self-assembled quantum dots", Phys. Rev. Lett. **84**, 733 (1999a).

Fry, P. W., I. E. Itskevich and D. J. Mowbray, "Quantum confined stark effect and permanent dipole moment of InAs-GaAs self-assembled quantum dots", Phys. Stat. Sol. (a) **178**, 269 (1999b).

Fuchs, M. and X. Gonze, "Accurate density functionals: Approaches using the adiabatic-connection fluctuation-dissipation theorem", Phys. Rev. B **65**, 235109 (2002).

Furche, F., "Molecular tests of the random phase approximation to the exchange-correlation energy functional", Phys. Rev. B **64**, 195120 (2001).

Gerardot, B. D., S. Seidl, P. A. Dalgarno and R. J. Warburton, "Manipulating exciton fine structure in quantum dots with a lateral electric field", Appl. Phys. Lett. **90**, 041101 (2007).

Ghosal, A., A. D. Güçlü, C. J. Umrigar, D. Ullmo and H. U. Baranger, "Correlation-induced inhomogenity in circular quantum dots", definition **2**, 336 (2006).

Girifalco, L. A., M. Hodak and R. S.Lee, "Carbon nanotubes, buckyballs, ropes, and a universal graphitic potential", Phys. Rev. B **62**, 13104 (2000).

Grossman, J. C., "Benchmark quantum Monte Carlo calculations", J. Chem. Phys. **117**, 1434 (2002).

Hammond, B. L., J. W. A. Lester and P. J. Reynolds, *Monte Carlo methods in Ab Initio quantum chemistry* (World Scientific, 1994).

Hansen, W., T. P. Smith, I. K. Y. Lee, J. A. Brum, C. M. Knoedler, J. M. Hong and D. P. Kern, "Zeeman bifurcation of quantum-dot spectra", Phys. Rev. Lett. **62**, 2168 (1989).

Harju, A., S. Siljamäki and R. M. Nieminen, "Two-electron quantum dot molecule: Composite particles and the spin phase diagram", Phys. Rev. Lett. **88**, 226804 (2002).

Harowitz, M., D. Shin and J. Shumway, "Path-integral quantum Monte Carlo techniques for self-assembled quantum dots", J. Low Temp. Phys. **140**, 211 (2005).

Helle, M., A. Harju and R. M. Nieminen, "Two-electron quantum-dot molecules in a magnetic field", Phys. Rev. B **72**, 205329 (2005).

Heller, W., U. Bockelmann and G.Abstreiter, "Electric-field effects on excitons in quantum dots", Phys. Rev. B **57**, 6270 (1998).

Jarrell, M. and O. Biham, "Dynamical approach to analytic continuation of quantum Monte Carlo data", Phys. Rev. Lett. **63**, 2504 (1989).

Kadantsev, E. and P. Hawrylak, "Theory of exciton fine structure in semiconductor quantum dots: Quantum dot anisotropy and lateral electric field", Phys. Rev. B **81**, 045311 (2010).

Kalos, M. H. and P. A. Whitlock, *Monte Carlo Methods Vol. 1* (John Wiley and Sons, 1986).

Korkusinski, M. and M. E. Reimer, "Engineering photon cascades from multiexciton complexes in a self-assembled quantum dot by a lateral electric field", Phys. Rev. B **79**, 035309 (2009).

Leitsmann, R. and F. Bechstedt, "Influence of the quantum confined stark effect on photoluminescence spectra of PbTe nanodots embedded in a CdTe matrix", Phys. Rev. B **80**, 165402 (2009).

Li, S.-S. and K. Chang, "Effective-mass theory for hierarchical self-assembly of GaAs/AlGaAs quantum dots", Phys. Rev. B **71**, 155301 (2005).

Li, S.-S. and J.-B. Xia, "Quantum-confined stark effects of InAs/GaAs self-assembled quantum dot", J. Appl. Phys. **88**, 7171 (2000).

Longe, P. and S. Bose, "Collective excitations in metallic graphene tubules", Phys. Rev. B **48**, 18 239 (1993).

Lorke, A. and J. P. Kotthaus, "Coupling of quantum dots on gaas", Phys. Rev. Lett. **64**, 2559 (1990).

Loss, D. and D. P. DiVincenzo, "Quantum computation with quantum dots", Phys. Rev. A **57**, 120 (1998).

Magro, W. R., D. M. Ceperley, C. Pierleoni and B. Bernu, "Molecular dissociation in hot, dense hydrogen", Phys. Rev. Lett. **76**, 1240 (1995).

Martel, R., V. Derycke, C. Lavoie, J. Appenzeller, K. K. Chan, J. Tersoff and P. Avouris, "Ambipolar electrical transport in semiconducting single-wall carbon nanotubes", Phys. Rev. Lett. **87**, 256805 (2001).

Mattis, D. C., *The Theory of Magnetism*, no. 17 in Springer series in solid-state science (Springer-Verlag, Berlin, 1981).

McDonald, P. G. and J. Shumway, "Lateral spatial switching of excitons using vertical electric fields in semiconductor quantum rings", Appl. Phys. Lett. **97**, 173101 (2010).

Meirav, U. and M. A. Kastner, "One-dimensional electron gas in GaAs: Periodic conductance oscillations as a function of density", Phys. Rev. B **40**, 5871 (1989).

Metropolis, N., A. W. Rosenbluth, M. N. Rosenbluth, A. H. Teller and E. Teller, "Equation of state calculations by fast computing machines", J. Chem. Phys. **21**, 1087 (1953).

Militzer, B. and E. L. Pollock, "Variational density matrix method for warm condensed matter and application to dense hydrogen", Phys. Rev. E **61**, 3470 (2000).

Moison, J. M., F. Houzay, F. Barthe and L. Leprince, "Self-organized growth of regular nanometer-scale InAs dots on GaAs", Appl. Phys. Lett. **64**, 196 (1993).

Mui, D. S. L., D. Leonard, L. A. Coldren and P. M. Petroff, "Surface migration induced self-aligned InAs islands grown by molecular beam epitaxy", Appl. Phys. Lett. **66**, 1620 (1995).

Ortiz, G., D. M. Ceperley and R. M. Martin, "New stochastic method for systems with broken time-reversal symmetry: 2D fermions in a magnetic field", Phys. Rev. Lett. **71**, 2777 (1993).

Pedersen, J. G., C. Flindt, N. A. Mortensen and A.-P. Jauho, "Failure of standard approximations of the exchange coupling in nanostrucures", Phys. Rev. B **76**, 125323 (2007).

Pierleoni, C., B. Bernu, D. M. Ceperley and W. R. Magro, "Equation of state of the hydrogen plasma by path integral Monte Carlo simulation", Phys. Rev. Lett. **73**, 2145 (1994).

Pitarke, J. M. and A. G. Eguiluz, "Surface energy of a bounded electron gas: Analysis of the accuracy of the local-density approximation via ab initio self-consistent-field calculations", Phys. Rev. B **57**, 6329 (1998).

Pokutnyi, S. I. and L. Jacak, "Stark effect in semiconductor quantum dots", J. Appl. Phys. **96**, 1115 (2004).

Raymond, S., J. P. Reynolds and J. L. Merz, "Asymmetric stark shift in AlInAs/AlGaAs self-assembled dots", Phys. Rev. B **58**, R13415 (1998).

Reimer, M. E., M. KorKusinski, D. Dalacu, J. Lefebvre and J. Lapointe, "Prepositioned single quantum dot in a lateral electric field", Phys. Rev. B **78**, 195301 (2008).

Ritter, S., P. Gartner, N. Baer and F. Jahnke, "Anomalous stark effect in semiconductor quantum dots", Phys. Rev. B **76**, 165302 (2007).

Roger, M., "Multiple exchange in He^3 and in the Wigner solid", Phys. Rev. B **30**, 11, 6432 (1984).

Rydberg, H., M. Dion and N. Jacobson, "Van der Waals density functional for layered structure", Phys. Rev. Lett. **91**, 126402 (2003a).

Rydberg, H., N. Jacobson, P. Hyldgaard, S. I. Simak, B. I. Lundqvist and D. C. Langreth, "Hard numbers on soft matter", Surf.Sci **532**, 606 (2003b).

Sabathil, M., S. Hackenbuchner, S. Birner, J. A. Majewski, P. Vogl and J. J. Finley, "Theory of vertical and lateral stark shifts of excitons in quantum dot", definition **4**, 1181 (2003).

Sanguinetti, S., M. Gurioli, E. Grilli and M. Guzzi, "Piezoelectric-induced quantum-confined stark effect in self-assembled InAs quantum dots grown on (n11) GaAs substrates", Appl. Phys. Lett. **77**, 1982 (2000).

Schmidt, K. E. and M. A. Lee, "High-accuracy Trotter-formula method for path integrals", Phys. Rev. E **51**, 6, 5495–5498 (1995).

Seafert, J., M. Obert, M. Scheibner, N. A. Gippius, G. Bacher and A.Forchel, "Stark effect and polarizability in a single CdSe/ZnSe quantum dot", Appl. Phys. Lett. **79**, 1033 (2001).

Sheng, W. and J.-P. Leburton, "Anomalous quantum-confined stark effects in stacked InAsGaAs self-assembled quantum dots", Phys. Rev. Lett. **88**, 167401 (2002).

Shumway, J. and D. M. Ceperley, "Path integral Monte Carlo simulations for fermion systems", J. Phys. IV France **10**, Pr5–3 (2000).

Tablero, C., “Quantum dot energy levels and spectrum for different geometries”, J. Appl. Phys. **106**, 074306 (2009).

Tans, S. J., A. R. M. Verschueren and C. Dekker, “Room-temperature transistor based on a single carbon nanotube”, Nature Phys. **393**, 49 (1998).

Thirumalai, D. and B. J. Berne, “On the calculation of time correlation functions in quantum systems: Path integral techniques”, J. Chem. Phys. **79**, 5029 (1983).

Thirumalai, D. and B. J. Berne, “Methods for simulating time correlation functions in quantum system”, Comp. Phys. Comm. **63**, 415 (1991).

Thouless, D. J., “Exchange in solid 3he and the heisenberg hamiltonian”, Proceedings of the Physical Society **86**, 5, 893 (1965).

Tomić, S. and N. Vukmirović, “Excitonic and biexcitonic properties of single GaN quantum dots modeled by 8-band k·p theory and configuration-interaction method”, Phys. Rev. B **79**, 245330 (2009).

Turchette, Q. A., W. L. C. J. Hood, H. Mabuchi and H. J. Kimble, “Measurement of conditional phase shifts for quantum logic”, Phys. Rev. Lett. **75**, 4710 (1995).

Wang, Y. and H. S. Djie, “Quantum-confined stark effect in interdiffused quantum dots”, Appl. Phys. Lett. **89**, 151104 (2006).

Warburton, R. J. and C. Schulhauser, “Giant permanent dipole moments of excitons in semiconductor nanostructures”, Phys. Rev. B **65**, 113303 (2002).

Widmann, F., J. Simon, B. Daudin, G. Feuillet, J. L. Rouviere and N. T. Pelekanos, “Blue-light emission from GaN self-assembled quantum dots due to giant peizoelectric effect”, Phys. Rev. B **58**, R15989 (1998).

Williamson, A. J., R. Q. Hood and J. C. Grossman, “Linear-scaling quantum Monte Carlo calculations”, Phys. Rev. Lett. **87**, 246406 (2001).

BIOGRAPHICAL SKETCH

Lei Zhang was born on August 3rd, 1984, in Shanghai, China. He received his B.S. in physics from Fudan University in 2006. While at Fudan university, he worked on conducting polymers systems with his advisor professor Sun, Xin. He began his graduate work at Arizona State University in the fall of 2006. While in Arizona, with the help of his advisor Dr. John Shumway, he used path integral Monte Carlo method to study several quantum many body systems including self-assembled quantum dots and quantum wires. His publication include:

Jesper Goor Pedersen, Lei Zhang, M J Gilbert, and J Shumway, "A path integral study of the role of correlation in exchange coupling of spins in double quantum dots and optical lattices," Phys.:Condens.Matter **22**, 145301 (2010).

Lei Zhang and J. Shumway, "Effects of correlation and hyperpolarizability on Stark shifts in InGaAs/GaAs dots," in preparation to submit to Phys. Rev. B, November, 2011.